國立交通大學

光電工程研究所

碩 士 論 文

光子晶體平板中的耦合共振光波導以及
指向性耦合器研究

Directional Couplers based on Coupled Resonant
Optical Waveguides in the Photonic Crystal Slab

研 究 生：李唯碩

指導教授：謝文峰　教授

中 華 民 國 一 百 年 六 月

光子晶體平板中的耦合共振光波導以及指向性耦合器研究

Directional Couplers based on Coupled Resonant Optical Waveguides in the Photonic Crystal Slab

研 究 生 ： 李唯碩　　Student : Wei-Shuo Li

指導教授 ： 謝文峰　教授　　Advisor : Prof. Wen-Feng Hsieh

國 立 交 通 大 學

光 電 工 程 研 究 所

碩 士 論 文

A Thesis

Submitted to Institute of Electro-Optical Engineering

College of Electrical and Computer Engineering

National Chiao Tung University

in partial Fulfillment of the Requirements

for the Degree of

Master

in

Electro-Optical Engineering

June 2011

Hsinchu, Taiwan, Republic of China

中 華 民 國 一 百 年 六 月

光子晶體平板中的耦合共振光波導以及指向性耦合器研究

研究生：李唯碩　　指導教授：謝文峰　教授

國立交通大學光電工程研究所碩士班

摘要

由光子晶體平板製成的耦合共振光波導以及指向性耦合器為一種能夠結合光減速、光通訊以及光學非線性效應等應用的結構。藉由廣義的緊密束縛理論所推導出來的解析方程式，我們可以用來分析此種結構的電磁場模態分布以及色散曲線。在此論文中主要針對兩種不同型態:介電柱以及空氣洞所形成的結構來加以分析，指向性耦合器基於波導之間的相對位置又可分為對立型以及交替型兩種。利用調整所設計結構中缺陷的大小，我們可以由數值模擬的方式來得到電場分布以及特徵頻率的變化，進而了解方程式中耦合係數的改變，因此色散曲線的變動趨勢亦可被預測。藉著比較平面波展開法的模擬結果，我們得知緊密束縛理論所推導出來的方程式可

以成功的運用在上述缺陷調變所引起的現象，除了可以用少量的參數來控制此種結構的色散行為外，亦可用來進行調變的規則設計。

Directional Couplers based on Coupled Resonant Optical Waveguides in the Photonic Crystal Slab

Student : Wei-Shuo Li Advisor : Prof. Wen-Feng Hsieh

Institute of Electro-Optical Engineering

National Chiao Tung University

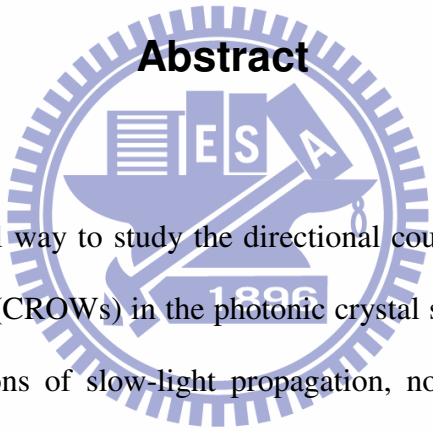

Abstract

We present an analytical way to study the directional couplers (DCs) based on coupled resonant optical waveguides (CROWs) in the photonic crystal slab (PCS). It holds potential for combining the applications of slow-light propagation, nonlinear optical processes and optical signal coupling in integrated photonic circuits. From the analytical equations derived by the extended tight-binding theory (TBT), we can obtain the dispersion relations and the electromagnetic (EM) mode distribution of a single PCS-CROW and the PCS-DCs. In the dielectric-rod structures, we find that the dispersion curves of the opposite-type PCS-DCs never cross and the frequency difference of them remains constant. Additionally, the dispersion relation of the alternating-type PCS-DCs with larger defects possess a crossing point, which will shift to the smaller wavevector and the higher frequency by increasing the defect radius. At this crossing point, the energy in one waveguide will never transfer into the other one and is also called the decoupling point. On the other hand, in the air-hole

structures, we know that the dispersion curves of both the opposite-type and alternating-type PCS-DCs have a decoupling point nearly fixed at a certain wavevector. Moreover, as increasing the wavevector, the frequency difference between the curves of the opposite-type PCS-DCs increases, and that of the alternating-type PCS-DCs increases and then decreases. In conclusion, the dielectric-rod structure can be used to form the demultiplexers, and the air-hole structures can be used to create the beam splitters. All of these theoretical analyses from the TBT agree well with the numerical ones using the plane-wave expansion method, and give the design rules for these kind of structures.

致謝

不知不覺都已經到了寫論文致謝的時候了，感覺時間真的是很不堪使用的事物，這個章節應該可以不用寫的太嚴肅吧。在提到實驗室之前必須要先感謝我的父母，過去很多的困難，不管是心情上或者是生活上的，都是依靠你們我才能順利走下去，也才有今天的我在這裡。當然我也知道自己很多時候的個性以及處理事情的方式給你們添了無數多的麻煩，很感謝你們願意這樣盡心的栽培我，感謝你們辛苦工作賺錢以及打點生活上的一切事情。很多事情我也不是不知道或者不願意表達出來，只是我也算是不擅長說話的那種人吧，也不知道應該說些什麼比較好，我知道你們會有機會看到這篇致謝，在這裡獻上我最真心的謝意。

提到實驗室方面，最感謝的是我的指導老師謝文峰教授，也很感激當初在同學許家瑋的牽線下有機會進到老師的實驗室，在這裡學術討論以及閒話家常等等都非常的自由，待了兩年後的現在，我是真的很喜歡這裡，這是真心話。想當初剛進實驗室時老師就很用心的帶著我讓我練習讀論文、作投影片以及練習會議報告的技巧，之後陸續像是進度報告、研討會的論文以及準備、畢業論文的修改以及畢業口試等等都很感激老師用心的幫忙我，這兩年來感覺自己無形中增進了不少能力以及視野。有時候在進度上拖到也會去壓縮到老師的時間，很多時候由於我不擅於言詞顯的比較悶一點，不好意思添了不少麻煩。之後還會繼續留在這裡念博士班，也請麻煩老師繼續指導了。

再來要謝謝光子晶體組的黃至賢學長，一開始我進到實驗室就是由學長帶的，感謝你對我這隻菜鳥新手的用心教導，很多時候遇到問題沒辦法解決只好來找你求救，前前後後也佔用到了不少時間。很感謝你在我什麼都不懂時花精神教我以及幫我處理很多狀況，另外也因為個人習慣的緣故在研究上的型態跟其他碩士班的同學不同，還有不少比較龜毛的地方，感謝學長時常可以配合我的情況，抱歉造成了你的困擾。也謝謝同樣是光子晶體組的柏毅學長，除了花時間讓我問問題外，也給了我不少研究上的參考資料。還有謝謝小豪學長、松哥、小郭學長在我對於研究方向以及未來的一些規劃不確定時給

了我不少很有建設性的建議。還有謝謝 Bogi 學長對我的關心，平常我並不習慣群體活動所以沒有說跟實驗室的成員混的非常熟，很謝謝你們願意特別來教導我以及提供我一些進行的方向。也謝謝厚仁學長跟智雅學姊的一些幫忙，之前博班入學以及畢業口試的一些相關準備和資料都是跟你們問的。還有感謝許智章學長，之前舉辦活動時麻煩你召集以及聯絡成大實驗室那裡的成員。

另外跟我同期的阿登、誌軒，謝謝你們有時候陪我聊天以及辦小型活動時一起聚會，雖然說我也不是常常待在實驗室混(應該說是沒在窩吧)所以並沒有說相處非常多，但是跟你們在一起讓我感覺很輕鬆(有時候也是 high 過頭了)，祝你們之後當兵以及職場也一切順利，以後有機會再聚聚吧。還有玠翰跟紹庭，也祝你們接下來的實驗順利成功，反正我還會在這邊陪你們到畢業啦，如果有我能幫的上忙的就來找我吧。另外全哥，也不知道你會不會看到這篇，或者你也快離開了(?)，有問題或需要參考資料都可以來找我沒差，祝好運。(這段我都搞不清楚到底是在寫致謝還是留言版了)

最後感謝這邊所有的人事物對我的幫助以及支持(當然我對新竹的食物跟天氣還是沒有好印象啦)，看到這篇的人，文筆不好也請多見諒，接下來幾年也請多多指教了。

李唯碩 于新竹交大 2011 年夏

Contents

List of Figures

Chapter 1 Introduction

1-1 Photonic crystal and Photonic crystal slab

1-1.1 Photonic crystal (PC)

In the last few decades, there have been many works on developing integrated photonic circuits, which hold potential to confine and control electromagnetic (EM) waves on the scale comparable to modern electronic devices and also can be created with integrated electronic circuits to improve the device performance. Photonic crystal (PC) is composed of multi -dimensional periodically arranged dielectric materials with large refraction index difference, which can provide a periodic dielectric function for light traveling. This kind of structures was first proposed by Eli Yablonovitch [1] and Sajeev John [2] in 1987, and have attracted a great deal of attentions because of low loss and high confinement of light, strong dispersive properties [3,4] and capability of fabricating in silicon substrates.

In the PCs, EM wave propagation is inhibited in certain ranges of frequencies, which is called photonic bandgap (PBG), and the photons with these frequencies can be trapped and guided by creating defects in the crystal lattice. These features are much analogous to the electronic band structures of semiconductors. In the PBG, the incident waves satisfy the Bragg condition and will be completely reflected owing to the vanish of corresponding eigenmodes, so the PC can be designed to prevent light propagating in certain direction with specific frequencies. Furthermore, if the interaction between light and the lattice is sufficiently strong, the PBG can extended to cover all possible directions, becoming a complete PBG [5], which can be used to form omni-directional reflectors [6] and can act as an efficient optical insulator. When we introduce some defects to break the translational

symmetry in the perfect PCs, which means to change the locations or sizes of the lattice points, that can provide extended defect modes with frequencies inside the PBG. Therefore, the light with certain frequencies or directions can easily be controlled in the structures.

These characteristics of the PBG offers many novel applications of optical mode confinement. For point defects, the defect modes can be strongly localized as in the optical resonant cavities with high quality factor [7]. On the other hand, by using line defects, the photonic crystal waveguides (PCWs) [8] can be created to restrict and to guide light from one position to another. Different from the index-guiding in the traditional total internal reflection (TIR) waveguides, whose disadvantages such as high energy loss and small bending angle will increase the scale of optical devices, the PCWs allow light to propagate in a medium with relatively low refraction index by the Bragg reflection, and can provide low energy loss even through a sharply bending [9] for wide range of frequencies.

1-1.2 Photonic crystal slab (PCS)

Generally, researches and applications are mainly about two-dimensional (2D) PC structures because the design and fabrication of which are relatively easy. However, for investigating the dispersion properties of practical PC devices with finite thickness, the structures called photonic crystal slab (PCS) should be considered, which promises easier fabrication using existing techniques. The PCS is a three-dimensional (3D) PC structure with 2D periodicity on a plane whose height is comparable to the lattice constant [10], and can use index guiding to confine light in the finite dimension, says the vertical direction. This structure can be simply classified into two types [11] : the dielectric rods in low index materials and the air holes in planar dielectric substrates. In general, the air-hole PCS is relatively easy to design and to avoid fabrication errors, so that is widely used to form the practical devices. To obtain the larger PBG in designing, the dielectric-rod and air-hole

structures are usually arranged with square lattice and triangular lattice individually, as shown in Fig. 1.1(a) and Fig. 1.1(b), where a is the lattice constant. Furthermore, to prevent from the multi-mode propagation in devices under operation frequencies [12], the air defects made by reducing the radius of dielectric rods or enlarging the radius of air holes (reducing the effective refraction index) are the better choices.

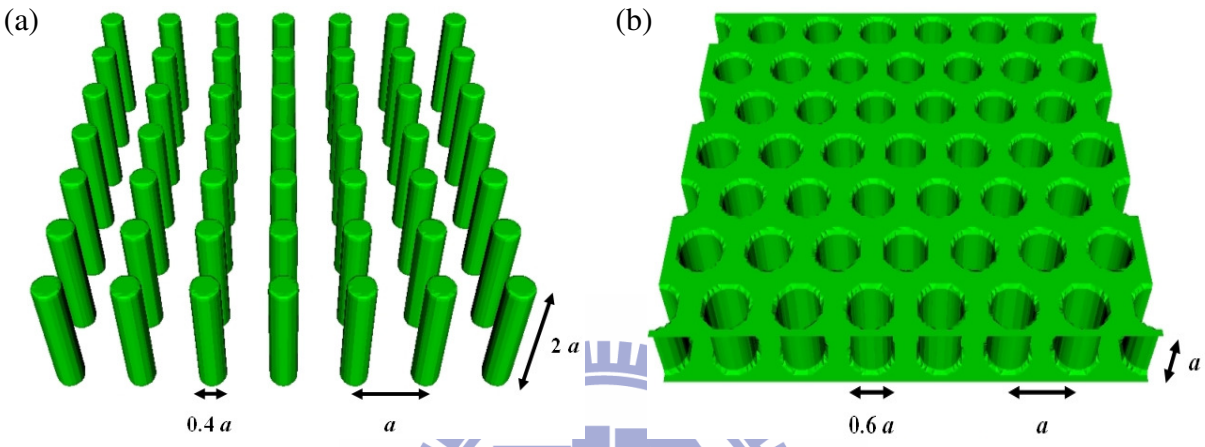

Fig. 1.1 Photonic crystal slabs made of (a) dielectric rods in air with a square lattice and (b) air holes in dielectric slab with a triangular lattice. The marked parameters are used in the simulations in Chapter 3.

In the PCS, owing to the lack of the translational symmetry in the vertical direction, there are no pure transverse-electric (TE) modes and transverse-magnetic (TM) modes, but rather the TE-like (even) modes and the TM-like (odd) modes, which are determined by that the electric fields are mainly parallel or vertical to the slab plane. Additionally, because of the finite thickness in the vertical direction, there exists a light line in the photonic band diagram. The propagation modes under this line can localize around the defects and be guided in waveguides. On the other hand, the radiation modes in the region above the light line will leak their energy outward the slab. Therefore, for the photonic devices, we should mainly focus on the propagation modes.

1-2 Coupled resonant optical waveguide (CROW)

The coupled resonant optical waveguide (CROW) is composed of linear periodic arrays of identical point-defect cavities in the PC. This kind of structures was first proposed and analyzed by Yariv *et al.* [13,14] in 1999. In the CROWs, electric fields are strongly localized in the defect cavities with high quality factor, and the propagation of EM waves can be accomplished by the evanescent-field coupling or photon hopping between the adjacent defects. Because of large group delay caused by the weak tunneling of waves among cavities, the group velocity of light in the CROWs can be several orders of magnitude smaller than that in bulk materials with the same refraction index, and the dispersion curve of defect modes is nearly flat. Such slow-light propagation has great significance for several devices of optical communication systems, such as group velocity dispersion (GVD) compensators [15,16], optical buffers [17] and delay lines [18,19]. Furthermore, the high-Q cavities lead to large field amplitude of defect modes, so the nonlinear interaction between photons and materials will be enhanced. This property is useful for many applications such as optical pulse propagation [20-22], soliton optics [23-25], holographic recording [26] and efficient second-harmonic generation (SHG) process [27,28].

1-3 Directional coupler (DC)

The directional coupler (DC), which can be created by placing a pair of parallel waveguides closely in the PC [29] as in Fig. 1.2, is a kind of optical components for mixing or separating the guided EM waves. For symmetric DCs, there are two dispersion curves corresponding to one odd parity mode and one even parity mode, with respect to the symmetry plane between the two waveguides. After an operation frequency is selected, the guided modes can be expressed as the linear combination of these eigenmodes, and the

coupling length can be defined as $\pi/\Delta k$, where Δk is the wavevector difference between the two dispersion curves. The light guided in one waveguide of the DC will be completely coupled into another one after travels a coupling length as in Fig. 1.3 (a). In some cases, the dispersion relations may have a crossing point due to the degeneracy of eigenmodes [11]. At this so-called decoupling point, the coupling length becomes infinite, so the power transfer between the two waveguides is eliminated as in Fig. 1.3 (b). These properties of optical signal coupling are especially important for integrated photonic circuits so the DC has been widely used in many devices, such as beam splitters [30,31], optical switches [32-34], add / drop filters [35], and wavelength multiplexers / demultiplexers [36,37]. Therefore, turning the decoupling point to get the proper coupling length at a certain range of frequencies is an important issue.

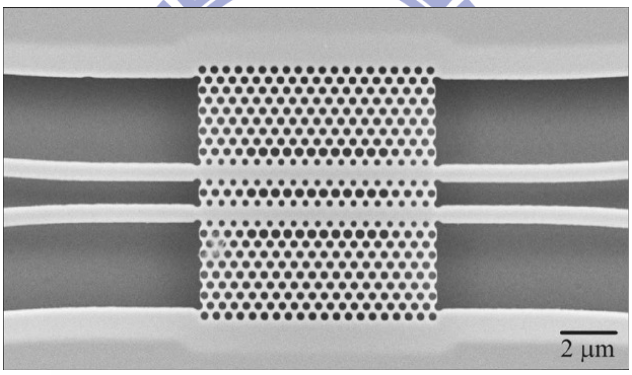

Fig. 1.2 An optical switch made of a directional coupler in the photonic crystal slab. [34]

(a) (b)

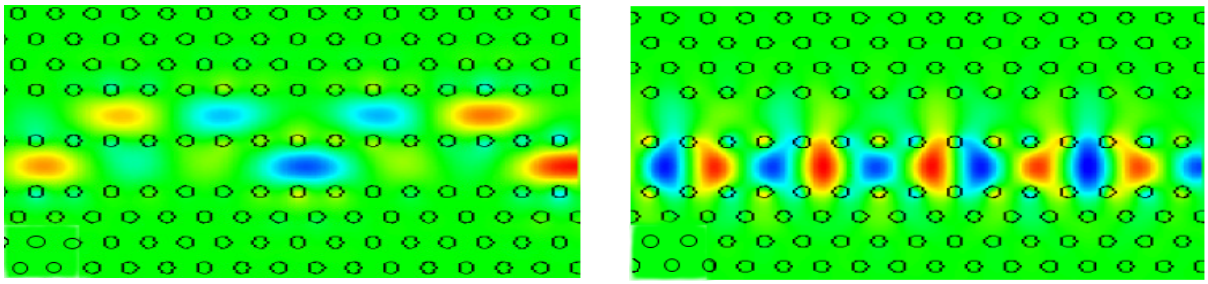

Fig. 1.3 Numerical simulation results of EM waves propagating in the DC (a) with a finite coupling length or (b) operated under the decoupling point (with an infinite coupling length).

1-4 Numerical methods

To investigate the EM wave propagation in such photonic devices, several numerical efficient algorithms such as the plane-wave expansion method (PWEM) [38,39] and the finite-difference time-domain (FDTD) method [40,41] are generally used to simulate the dispersion characteristics of the PC structures.

1-4.1 Plane-wave expansion method (PWEM)

The PWEM is good at analyzing the photonic band structures and waveguide modes for a specific polarization of infinite periodic structures. It is operated by formulating and solving the eigenvalue equations of the EM fields.

From the Maxwell's equations, we know that

$$\nabla \cdot \mathbf{D}(\mathbf{r}, t) = \rho(\mathbf{r}, t) \tag{1.1}$$

$$\nabla \times \mathbf{E}(\mathbf{r}, t) = -\partial \mathbf{B}(\mathbf{r}, t) / \partial t \tag{1.2}$$

$$\nabla \cdot \mathbf{B}(\mathbf{r}, t) = 0 \tag{1.3}$$

$$\nabla \times \mathbf{H}(\mathbf{r}, t) = \partial \mathbf{D}(\mathbf{r}, t) / \partial t + \mathbf{J}(\mathbf{r}, t), \tag{1.4}$$

where $\mathbf{E}(\mathbf{r}, t)$ is the electric field intensity, $\mathbf{H}(\mathbf{r}, t)$ is the magnetic field intensity, $\mathbf{D}(\mathbf{r}, t)$ is the electric flux density, $\mathbf{B}(\mathbf{r}, t)$ is the magnetic flux density, $\rho(\mathbf{r}, t)$ is the electric charge density, $\mathbf{J}(\mathbf{r}, t)$ is the electric current density, and $\boldsymbol{r}$ is the spatial coordinate, respectively. Assume the dielectric materials are source-free, transparent, linear, isotropic, non-dispersive, and non-magnetic, these equations can be written as

$$\nabla \cdot \mathbf{E}(\mathbf{r}, t) = 0 \tag{1.5}$$

$$\nabla \times \mathbf{E}(\mathbf{r}, t) = -\mu_0 [\partial \mathbf{H}(\mathbf{r}, t) / \partial t] \tag{1.6}$$

$$\nabla \cdot \mathbf{H}(\mathbf{r}, t) = 0 \tag{1.7}$$

$$\nabla \times \mathbf{H}(\mathbf{r}, t) = \varepsilon_0 \varepsilon_r(\mathbf{r}) [\partial \mathbf{E}(\mathbf{r}, t) / \partial t], \tag{1.8}$$

where ε_0 is the permittivity of the free space, $\varepsilon_r(\mathbf{r})$ is the relative permittivity, and μ_0 is the permeability of the free space. In form of time-harmonic electric fields and magnetic fields

$$\mathbf{E}(\mathbf{r}\ ,\ t) = \mathbf{E}(\mathbf{r})\ \exp(\mathrm{i}\omega t) \tag{1.9}$$

$$\mathbf{H}(\mathbf{r}\ ,\ t) = \mathbf{H}(\mathbf{r})\ \exp(\mathrm{i}\omega t)\ , \tag{1.10}$$

we substitute Eq. (1.9) and Eq. (1.10) into Eq. (1.6) and Eq. (1.8), and obtains

$$\bigtriangledown \times \mathbf{E}(\mathbf{r}) + \mathrm{i}\omega\mu_0\ \mathbf{H}(\mathbf{r}) = 0 \tag{1.11}$$

$$\bigtriangledown \times \mathbf{H}(\mathbf{r}) - \mathrm{i}\omega\varepsilon_0\ \varepsilon_r(\mathbf{r})\ \mathbf{E}(\mathbf{r}) = 0\ . \tag{1.12}$$

By calculating the curl of Eq. (1.12) :

$$\bigtriangledown \times [[\varepsilon_r(\mathbf{r})]^{-1}\ \bigtriangledown \times \mathbf{H}(\mathbf{r})] - \mathrm{i}\omega\varepsilon_0\ [\bigtriangledown \times \mathbf{E}(\mathbf{r})] = 0 \tag{1.13}$$

and using Eq. (1.11), we get

$$\bigtriangledown \times [[\varepsilon_r(\mathbf{r})]^{-1}\ \bigtriangledown \times \mathbf{H}(\mathbf{r})] = \omega^2\ \varepsilon_0\ \mu_0\ \mathbf{H}(\mathbf{r})\ . \tag{1.14}$$

With the speed of light in the free space $c_0 = 1/\sqrt{(\varepsilon_0\ \mu_0)}$, Eq. (1.14) becomes

$$\Theta_{\mathrm{H}}\ \mathbf{H}(\mathbf{r}) = \bigtriangledown \times [[\varepsilon_r(\mathbf{r})]^{-1}\ \bigtriangledown \times \mathbf{H}(\mathbf{r})] = (\omega\ /\ c_0)^2\ \mathbf{H}(\mathbf{r})\ , \tag{1.15}$$

where Θ_{H} is the hermitian operator. Similarly, we can obtain from Eq. (1.11)

$$\Theta_{\mathrm{E}}\ \mathbf{E}(\mathbf{r}) = [\varepsilon_r(\mathbf{r})]^{-1}\ \bigtriangledown \times [\bigtriangledown \times \mathbf{E}(\mathbf{r})] = (\omega\ /\ c_0)^2\ \mathbf{E}(\mathbf{r})\ . \tag{1.16}$$

Because the PC is a periodic structure, the dielectric function $\varepsilon(\mathbf{r})$ can be written as

$$\varepsilon_r(\mathbf{r}) = \varepsilon_r(\mathbf{r} + \mathbf{T}) \tag{1.17}$$

$$\mathbf{T} = u_1\ \mathbf{a}_1 + u_2\ \mathbf{a}_2 + u_3\ \mathbf{a}_3\ , \tag{1.18}$$

where $\mathbf{T}$ is the lattice translation vector, $\{\mathbf{a}_\mathrm{i}\}$ are primitive translation vectors, u_1, u_2 and u_3 are integers, respectively. Therefore, we can also define the reciprocal lattice vector as

$$\mathbf{G} = m_1\ \mathbf{b}_1 + m_2\ \mathbf{b}_2 + m_3\ \mathbf{b}_3\ , \tag{1.19}$$

where $\{\mathbf{b}_\mathrm{i}\}$ are primitive translation vectors, m_1, m_2 and m_3 are integers, and

$$\mathbf{a}_\mathrm{i}\ \cdot\ \mathbf{b}_\mathrm{j} = 2\pi\ \delta_{\mathrm{ij}} \tag{1.20}$$

with the Kronecker's delta function δ_{ij}. By expanding the $[\varepsilon(\mathbf{r})]^{-1}$ into the Fourier series as

$$[\varepsilon_r(\mathbf{r})]^{-1} = \sum_{\boldsymbol{G}} \kappa(\mathbf{G})\ \exp(\mathrm{i}\mathbf{G}\ \cdot\ \mathbf{r}) \tag{1.21}$$

$$\kappa(\mathbf{G}) = (1\ /\ V_C) \int_{\mathrm{cell}} [\varepsilon_r(\mathbf{r})]^{-1}\ \exp(-\mathrm{i}\mathbf{G}\ \cdot\ \mathbf{r})\ \mathrm{dV}\ , \tag{1.22}$$

where V_C is the volume of an unit cell. Applying the Bloch's theorem to the fields, we derive the following eigenfunctions for Eq. (1.15) and Eq. (1.16)

$$\mathbf{E}_{kn}(\mathbf{r}) = \sum_{\mathbf{G}} \mathbf{E}_{kn}(\mathbf{G}) \exp[i(\mathbf{k} + \mathbf{G}) \cdot \mathbf{r}] \tag{1.23}$$

$$\mathbf{H}_{kn}(\mathbf{r}) = \sum_{\mathbf{G}} \mathbf{H}_{kn}(\mathbf{G}) \exp[i(\mathbf{k} + \mathbf{G}) \cdot \mathbf{r}] , \tag{1.24}$$

where $\boldsymbol{k}$ indicates the wavevector and n denotes the index of photonic bands. By substituting Eq. (1.23) and Eq. (1.24) into Eq. (1.15) and Eq. (1.16), we can obtain the eigenvalue equations as

$$\sum_{\mathbf{G'}} \kappa(\mathbf{G} - \mathbf{G'}) (\mathbf{k} + \mathbf{G'}) \times [(\mathbf{k} + \mathbf{G'}) \times \mathbf{E}_{kn}(\mathbf{G'})] = -(\omega_{kn} / c_0)^2 \mathbf{E}_{kn}(\mathbf{G}) \tag{1.25}$$

$$\sum_{\mathbf{G'}} \kappa(\mathbf{G} - \mathbf{G'}) (\mathbf{k} + \mathbf{G}) \times [(\mathbf{k} + \mathbf{G'}) \times \mathbf{H}_{kn}(\mathbf{G'})] = -(\omega_{kn} / c_0)^2 \mathbf{H}_{kn}(\mathbf{G}) , \tag{1.26}$$

where ω_{kn} is the eigenfrequency for the specific fields $\mathbf{E}_{kn}(\mathbf{r})$ and $\mathbf{H}_{kn}(\mathbf{r})$. By solving these two equations numerically, we can obtain the photonic band diagram of the PC structure.

1-4.2 Finite-difference time-domain (FDTD) method

On the other hand, the FDTD method is regularly used to estimate the transmission and reflection spectra for computational electromagnetic problems, and can deal with the structures with finite boundary, which is hard to be done by the PWEM. This method is directly derive from the Maxwell's equations in the time-domain on a space grid to study the characteristics of EM wave propagation at different time, and the fields are obtained by iterating each other in time and spatial domains. Additionally, it can avoid mathematical complexities of solving frequency-domain problems.

In the isotropic and lossless medium, Eq. (1.6) and Eq. (1.8) are equivalent to the following scalar equations in the rectangular coordinate system:

$$\varepsilon(\mathbf{r}) (\partial E_x / \partial t) = (\partial H_z / \partial y) - (\partial H_y / \partial z) \tag{1.27}$$

$$\varepsilon(\mathbf{r}) (\partial E_y / \partial t) = (\partial H_x / \partial z) - (\partial H_z / \partial x) \tag{1.28}$$

$$\varepsilon(\mathbf{r}) (\partial E_z / \partial t) = (\partial H_y / \partial x) - (\partial H_x / \partial y) \tag{1.29}$$

$$\mu_0 (\partial H_x / \partial t) = (\partial E_y / \partial z) - (\partial E_z / \partial y) \tag{1.30}$$

$$\mu_0 (\partial H_y / \partial t) = (\partial E_z / \partial x) - (\partial E_x / \partial z) \tag{1.31}$$

$$\mu_0 (\partial H_z / \partial t) = (\partial E_x / \partial y) - (\partial E_y / \partial x) , \tag{1.32}$$

where $\mathbf{E}(\mathbf{r} , t) = (E_x , E_y , E_z)$ and $\mathbf{H}(\mathbf{r} , t) = (H_x , H_y , H_z)$. To denote a grid point of space as

$$(i , j , k) = (i\Delta x , j\Delta y , k\Delta z) \tag{1.33}$$

for any function of space and time, we assume

$$F(i\Delta x , j\Delta y , k\Delta z , n\Delta t) = F^n(i , j , k), \tag{1.34}$$

where Δx , Δy , and Δz are spatial discretizations, Δt is the time step, and i, j, k, n are integers. By applying the central-difference approximations for both the spatial and temporal differential equations, we obtain

$$\partial F^n(i , j , k) / \partial x = [F^n(i + 1/2 , j , k) - F^n(i - 1/2 , j , k)]/\Delta x \tag{1.35}$$

$$\partial F^n(i , j , k) / \partial y = [F^n(i , j + 1/2 , k) - F^n(i , j - 1/2 , k)]/\Delta y \tag{1.36}$$

$$\partial F^n(i , j , k) / \partial z = [F^n(i , j , k + 1/2) - F^n(i , j , k - 1/2)]/\Delta z \tag{1.37}$$

$$\partial F^n(i , j , k) / \partial t = [F^{n+1/2}(i , j , k) - F^{n-1/2}(i , j , k)]/\Delta t . \tag{1.38}$$

Substituting Eqs. (1.35) – (1.38) into Eq. (1.27), we can get the following finite-difference time-domain expression for the x component of electric fields :

$$E_x{}^{n+1}(i + 1/2 , j , k) = E_x{}^n(i + 1/2 , j , k)$$
$$+ [\Delta t / \varepsilon(\mathbf{r})] \{ [H_z{}^{n+1/2}(i + 1/2 , j + 1/2 , k) - H_z{}^{n+1/2}(i + 1/2 , j - 1/2 , k)] / \Delta y$$
$$- [H_y{}^{n+1/2}(i + 1/2 , j , k + 1/2) - H_y{}^{n+1/2}(i + 1/2 , j , k - 1/2)] / \Delta z \}. \tag{1.39}$$

Through the same procedures, we can obtain

$$E_y{}^{n+1}(i , j + 1/2 , k) = E_y{}^n(i , j + 1/2 , k)$$
$$+ [\Delta t / \varepsilon(\mathbf{r})] \{ [H_x{}^{n+1/2}(i , j + 1/2 , k + 1/2) - H_x{}^{n+1/2}(i , j + 1/2 , k - 1/2)] / \Delta z$$
$$- [H_z{}^{n+1/2}(i + 1/2 , j + 1/2 , k) - H_z{}^{n+1/2}(i - 1/2 , j + 1/2 , k)] / \Delta x \}, \tag{1.40}$$

$$H_z{}^{n+1/2}(i + 1/2 , j + 1/2 , k) = H_z{}^{n-1/2}(i + 1/2 , j + 1/2 , k)$$
$$+ (\Delta t / \mu_0) \{ [E_x{}^n(i + 1/2 , j + 1 , k) - E_x{}^n(i + 1/2 , j , k)] / \Delta y$$
$$- [E_y{}^n(i + 1 , j + 1/2 , k) - E_y{}^n(i , j + 1/2 , k)] / \Delta x \}, \tag{1.41}$$

$$E_z^{n+1}(i, j, k+1/2) = E_z^{n}(i, j, k+1/2)$$

$$+ [\Delta t / \varepsilon(\mathbf{r})] \{ [H_y^{n+1/2}(i+1/2, j, k+1/2) - H_y^{n+1/2}(i-1/2, j, k+1/2)] / \Delta x$$

$$- [H_x^{n+1/2}(i, j+1/2, k+1/2) - H_x^{n+1/2}(i, j-1/2, k+1/2)] / \Delta y \}, \quad (1.42)$$

$$H_x^{n+1/2}(i, j+1/2, k+1/2) = H_x^{n-1/2}(i, j+1/2, k+1/2)$$

$$+ (\Delta t / \mu_0) \{ [E_y^{n}(i, j+1/2, k+1) - E_y^{n}(i, j+1/2, k)] / \Delta z$$

$$- [E_z^{n}(i, j+1, k+1/2) - E_z^{n}(i, j, k+1/2)] / \Delta y \}, \quad (1.43)$$

$$H_y^{n+1/2}(i+1/2, j, k+1/2) = H_y^{n-1/2}(i+1/2, j, k+1/2)$$

$$+ (\Delta t / \mu_0) \{ [E_z^{n}(i+1, j, k+1/2) - E_z^{n}(i, j, k+1/2)] / \Delta x$$

$$- [E_x^{n}(i+1/2, j, k+1) - E_x^{n}(i+1/2, j, k)] / \Delta z \}. \quad (1.44)$$

Eqs. (1.39) – (1.41) are the finite difference equations for the transverse electric (TE) waves, and Eqs. (1.42) – (1.44) are the equations for the transverse magnetic (TM) waves. In addition, Fig. 1.4 is the Yee's cell used to describe the various field components for the FDTD method that assume the components of electric fields are in the middle of the edges and of magnetic fields are in the center of the faces to satisfy the curl relations of the Maxwell's equations.

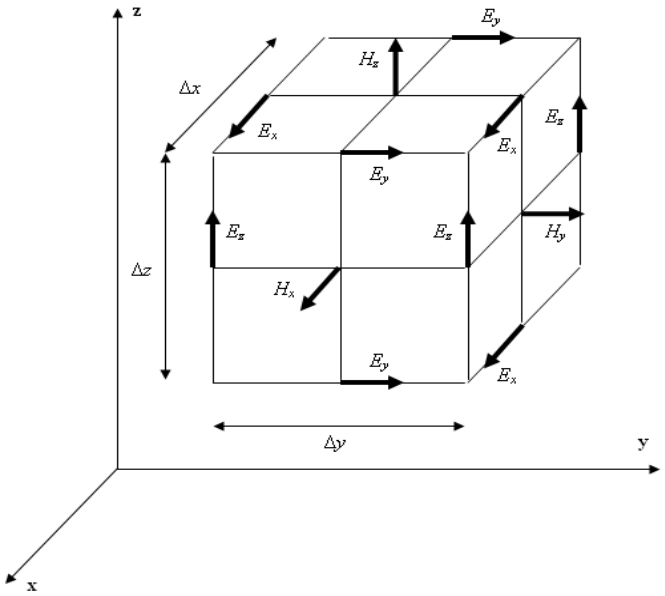

Fig. 1.4 Components of the electric fields and the magnetic fields in the Yee's cell.

When using the FDTD method, we must set ideal absorbing boundary layers to keep the calculating region from the reflection of EM waves, and the boundary condition of perfect matched layers are the most efficient and widely used. Additionally, in order to ensure the values converge to stable solutions, the time step should satisfy the restriction :

$$c_0 \Delta t \leq 1 / \sqrt{[(\Delta x)^{-2} + (\Delta y)^{-2} + (\Delta z)^{-2}]} . \quad (1.45)$$

For increasing the simulation accuracy, a smaller grid size should be considered, but the appropriate time step is also reduced, which makes the time-consuming in the computation.

1-5 Motivation

The CROWs made by periodic arrays of point defects in the PC will lead to a large group delay for the propagation of EM waves, and the defects can act as the optical cavities with high quality factor. Therefore, the group velocity of light can be reduced by several orders of magnitude, and the nonlinear interaction between the fields and materials can be enhanced. On the other hand, the DC consist of a pair of waveguides in the PC support two dispersion curves with one odd mode and one even mode, and can be used to mix or separate the optical signals of different frequencies by controlling the coupling length. In the symmetric structures, these two dispersion curves may cross at a so-called decoupling point, and the EM waves propagate under this point will have no energy coupling between the two waveguides. For integrated photonic circuits, combining different types of structures is an important issue, because that can hold more abilities and improve the performance of the whole systems. In addition, 3D structures as the slab should be considered to approach actual devices. To our best of knowledge, there is no research demonstrating the DCs based on CROWs in the PCS, which holds potential to combine the applications of slow-light propagation, nonlinear optical processes and optical signal coupling. Therefore, it is worth discussing the dispersion behaviors and providing the effective models for this kind of structures.

To design such photonic devices, numerical methods such as the PWEM and the FDTD method are regularly used to simulate the band diagram and the characteristics of EM wave propagation. However, these methods cannot provide a direct physical insight or a good explanation for the simulation results, and they also require concentrated computing to reach the coupling behaviors within the designed models. In the CROWs, the strong localization of electric fields and the weak tunneling of EM waves have much in common with the electronic transport in crystalline solids, which possess strong periodic potential from the localized lattice atoms. Therefore, the tight-binding theory (TBT) in solid-state physics [42,43] can be used to express the eigenmodes in the CROWs, and the simple equations of the dispersion relation can be derived analytically, which have the ability to describe the coupling effects between the defect cavities [13]. This method and the derived equations have been successively used in many studies of both linear and nonlinear optical properties of the CROW structures [13-16, 19-22, 24-27], so we anticipate using it to investigate and provide a design concept on our structures.

1-6 Organization of the thesis

In this thesis, we first introduce the extended TBT to derive the analytical equations in Chapter 2, which can be used to describe the dispersion relations and the mode distribution for a single CROW and symmetric DCs made of CROWs in the PCS. We call these structures the PCS-CROWs and the PCS-DCs. The PCS-DCs can be classified into four types from the relative positions of the PCS-CROWs and the composition of the PCS. Then, by modifying the size of the defects in the designed structures, we can obtain the variation of electric fields among the cavities, and realize the changes of the parameters in the derived equations that influence on the dispersion curves. In Chapter 3, we first discuss the simulation errors due to the finite size of the super cell in the 3D PWEM, and the difference

between the simulation results of 2D and 3D structures. Then, we show that the dispersion behaviors of the PCS-CROWs and the PCS-DCs analytically predicted by the TBT agree well with the numerical results simulated by the PWEM, and the design rules of these structures are given. Additionally, we also discuss the possible applications for the different types of PCS-DCs. Finally, the conclusion and perspectives are presented in Chapter 4.

Chapter 2 Theoretical Analysis

2-1 Tight-binding theory (TBT)

The tight-binding theory (TBT) was first used in solid-state physics to describe the electronic transport in a strong periodic potential from the lattice atoms. In these atoms, electrons are tightly bound around the nucleus, and their wavefunctions will overlap due to the small separation between lattice points. As these atoms approaching, the Coulomb interaction of the nuclei and electrons will split the energy levels and form the electronic band structures. By the tight-binding approximation, the propagation modes of electron waves of the overall system are closely related to the eigenmodes of individual lattice atoms, and the influences between different lattice points are considered as small perturbations. Additionally, this method also has been successfully used in various photonic structures similar to the crystalline solids.

In this chapter, we use the extended TBT to analyze the coupling effects of a single CROW in the PCS (PCS-CROW) and the DCs made of CROWs in the PCS (PCS-DCs). This method assume that the strongly localized electric fields around an isolated defect are not perturbed much by the presence of the other defects, and the finite coupling should exist between successive defect cavities. In addition, the eigenmodes of each point defects are assumed as single modes, and the total fields of propagation modes can be expressed as the linear combination of these defect modes. Hence, the analytical equations of the dispersion relations of these structures can be directly derived, and the design rules of which can be controlled by only few parameters about the coupling strength and the eigenfrequency of these defect cavities.

2-2 TBT in a single PCS-CROW

We begin our analysis by considering two cases : a single CROW consist of reduced rods in the PCS with a square lattice of dielectric rods in air ; and a single CROW consist of enlarged holes in the PCS with a triangular lattice of air holes in a dielectric slab, as shown in Fig. 2.1(a) and Fig. 2.1(b). The lattice constant of the PCS is *a*, and the propagation direction of waveguides are along *x*-direction. In addition, the dielectric-rod PCS with square lattice and the air-hole PCS with triangular lattice can lead to relatively large PBG to obtain the behaviors of the defect bands, and the air defects made by reduced rods or enlarged holes can support the single-mode propagation.

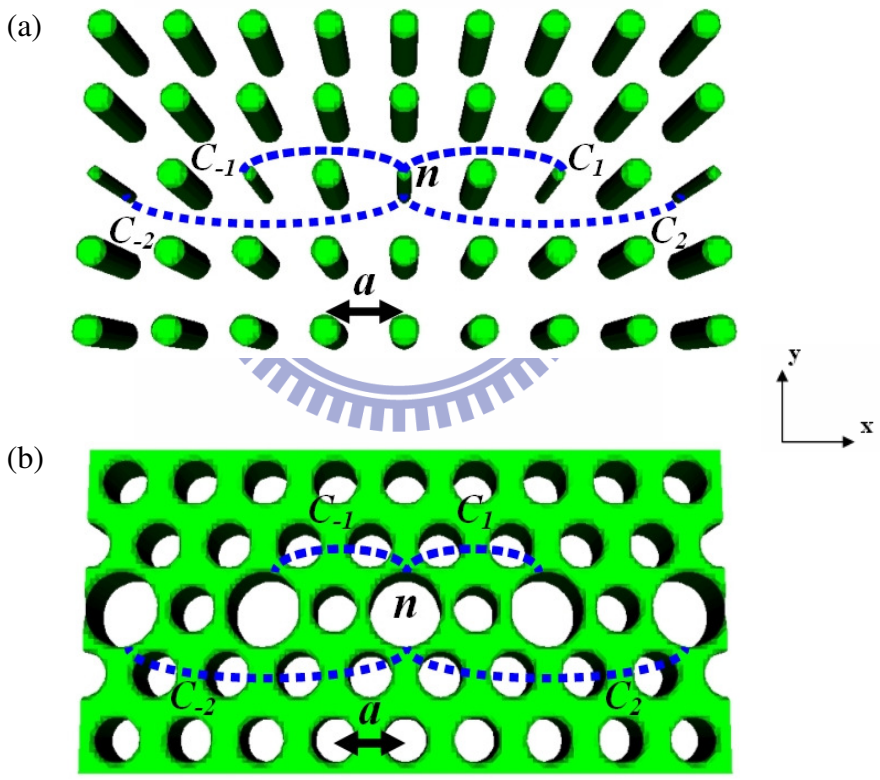

Fig. 2.1 Structures of a single CROW made in the PCS (a) with a square lattice of dielectric rods in air and (b) with a triangular lattice of air holes in dielectric slab. *a* is the lattice constant, and C_1 , C_{-1} , C_2 , C_{-2} are the coupling coefficients between the point defects.

By applying the TBT, we assume that each EM mode of the point defects has an eigenfrequency ω_0 and is unable to be affected much by the presence of the other defects [13]. The mode of an isolated defect is given by $\mathbf{E}(\mathbf{r}, t) = \mathbf{E}_0(\mathbf{r})\, u(t)$, where $\mathbf{E}_0(\mathbf{r})$ and $u(t) = U_0 \exp(-i\omega_0 t)$ are the spatial and the temporal amplitudes of the cavity eigenmode, and U_0 is a constant amplitude. For the perturbed mode at defect site n, these amplitudes are $\mathbf{E}_n(\mathbf{r}) = \mathbf{E}_0(\mathbf{r} - 2na\mathbf{x})$ and $u_n(t)$, where $\mathbf{x}$ is the unit direction vector along the waveguide. Therefore, the total field of the CROW is the summation of all defect modes as $\mathbf{E}(\mathbf{r}, t) = \sum_n \mathbf{E}_n(\mathbf{r})\, u_n(t)$. Due to the weak coupling of the cavities, we consider the influences only by the nearest and the next-nearest neighboring defects, and the coupled equation to relate u_n and $u_{n\pm p}$ can be derived by using the slowly varying amplitude approximation [23] as

$$i\,(\partial u_n / \partial t) = (\omega_0 - C_0)\, u_n - \sum_{p=1}^{2} C_p\, (u_{n+p} + u_{n-p})\,, \tag{2.1}$$

where C_0 represents a small shift to the eigenfrequency of a single point defect due to the dielectric perturbation from the neighboring defects, and $C_p = C_{-p}$ is the coupling coefficient between defects at sites n and $n \pm p$. This parameter is defined as

$$C_p = \frac{\omega_0 \int_{-\infty}^{\infty} \Delta\varepsilon(\mathbf{r})\, \mathbf{E}_0(\mathbf{r} - 2na\mathbf{x}) \cdot \mathbf{E}_0(\mathbf{r} - 2(n \pm p)a\mathbf{x})\, d^3r}{\int_{-\infty}^{\infty} [\mu_0 |\mathbf{H}_0(\mathbf{r} - 2na\mathbf{x})|^2 + \varepsilon(\mathbf{r}) |\mathbf{E}_0(\mathbf{r} - 2na\mathbf{x})|^2]\, d^3r}\,, \tag{2.2}$$

which is proportional to the electric field amplitudes at defect sites, and $\Delta\varepsilon(\mathbf{r}) = \varepsilon'(\mathbf{r}) - \varepsilon(\mathbf{r})$ is the difference of dielectric constants between the perturbed system (coupled defects) $\varepsilon'(\mathbf{r})$ and the unperturbed system (an isolated defect) $\varepsilon(\mathbf{r})$, and $p = 0, 1, 2$. Let $u_n(t) = U \exp(2ikna - i\omega_1 t)$, where k is the propagation constant, and U is the constant amplitude. By substituting this into Eq. (2.1), the dispersion relation of a single PCS-CROW can be written as

$$\omega_1(k) = (\omega_0 - C_0) - \sum_{p=1}^{2} 2C_p \cos(2pka), \tag{2.3}$$

where C_0 stands for the relative shift for all wavevectors to the eigenfrequency of a single point defect, and C_p leads to the sinusoidal modulation of dispersion curves.

2-3 TBT in the PCS-DCs

When a second identical PCS-CROW is created to form a symmetric DC, that can be classified into two types from the relative positions of the two waveguides. One is the opposite-type PCS-DC, where the defect sites of both the PCS-CROWs are the same (n, $n \pm 1$, $n \pm 2$, ... etc) as shown in Fig. 2.2(a) and Fig. 2.2(b). The other is the alternating-type PCS-DC, where the defect sites of one PCS-CROW (n, $n \pm 1$, $n \pm 2$, ... etc) and of another one ($n \pm 1/2$, $n \pm 3/2$, ... etc) are shown in Fig. 2.3(a) and Fig. 2.3(b). In addition, the distance between the two waveguides is D, and the slab plane is xy-plane.

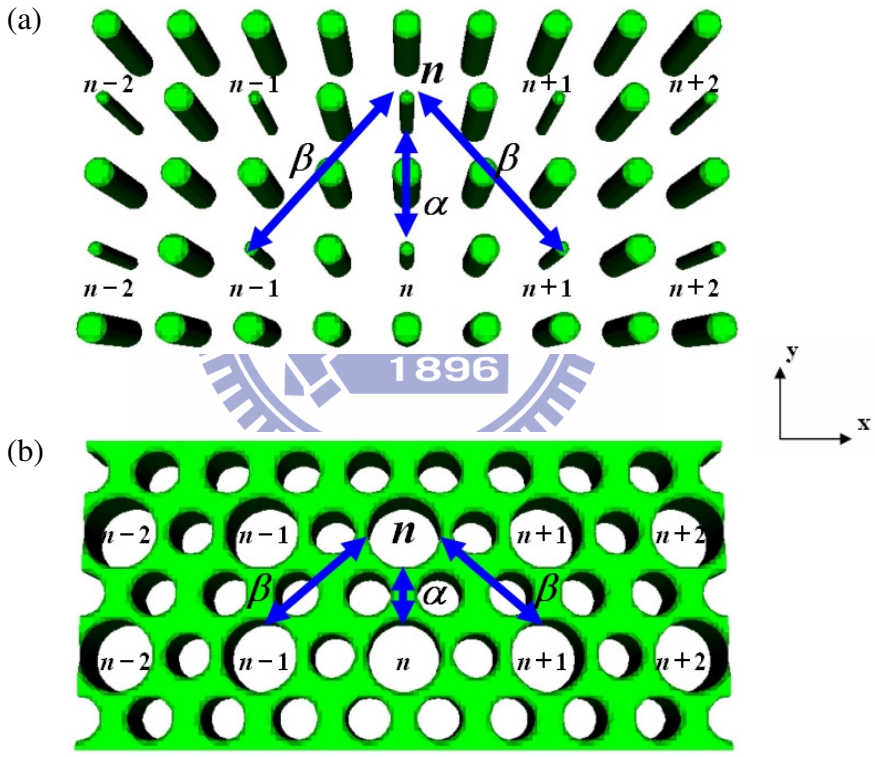

Fig. 2.2 Structures of the opposite-type PCS-DCs made of (a) a square lattice of dielectric rods in air, and (b) a triangular lattice of air holes in dielectric slab. α and β are the coupling coefficients of one PCS-CROW induced by the nearest neighboring and the next-nearest neighboring defects of another PCS-CROW.

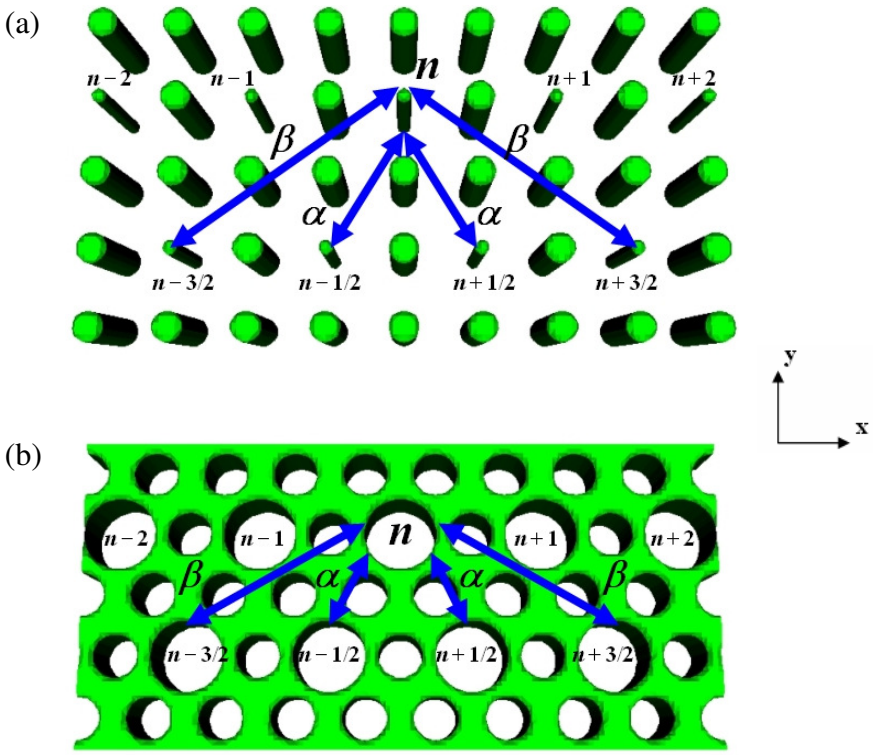

Fig. 2.3 Structures of the alternating-type PCS-DCs made of (a) a square lattice of dielectric rods in air, and (b) a triangular lattice of air holes in dielectric slab.

2-3.1 Opposite-type PCS-DC

In the opposite-type PCS-DC, $u_n(t)$ and $v_n(t)$ are the temporal amplitudes of the perturbed mode at defect site n of the two PCS-CROWs, and the coupled equation can be derived in the same way as

$$\mathrm{i}\,(\partial u_n / \partial t) = (\omega_0 - C_0)\,u_n - \sum_{p=1}^{2} C_p\,(u_{n+p} + u_{n-p}) - \alpha\,v_n - \beta\,(v_{n+1} + v_{n-1}) \qquad (2.4)$$

$$\mathrm{i}\,(\partial v_n / \partial t) = (\omega_0 - C_0)\,v_n - \sum_{p=1}^{2} C_p\,(v_{n+p} + v_{n-p}) - \alpha\,u_n - \beta\,(u_{n+1} + u_{n-1})\,, \qquad (2.5)$$

where α and β are the coupling coefficients of a defect at site n in one PCS-CROW induced by the nearest neighboring (at site n) and the next-nearest neighboring (at sites $n \pm 1$) defects of another PCS-CROW, and have the same form as C_p in Eq. 2.2. These coupling coefficients are defined as

$$\alpha = \frac{\omega_0 \int_{-\infty}^{\infty} \Delta\varepsilon(\mathbf{r})\, \mathbf{E}_0(\mathbf{r} - 2na\mathbf{x}) \cdot \mathbf{E}_0(\mathbf{r} - 2na\mathbf{x} + D\mathbf{y})\, d^3r}{\int_{-\infty}^{\infty} [\mu_0 |\mathbf{H}_0(\mathbf{r} - 2na\mathbf{x})|^2 + \varepsilon(\mathbf{r}) |\mathbf{E}_0(\mathbf{r} - 2na\mathbf{x})|^2]\, d^3r} \tag{2.6}$$

$$\beta = \frac{\omega_0 \int_{-\infty}^{\infty} \Delta\varepsilon(\mathbf{r})\, \mathbf{E}_0(\mathbf{r} - 2na\mathbf{x}) \cdot \mathbf{E}_0(\mathbf{r} - 2(n \pm 1)a\mathbf{x} + D\mathbf{y})\, d^3r}{\int_{-\infty}^{\infty} [\mu_0 |\mathbf{H}_0(\mathbf{r} - 2na\mathbf{x})|^2 + \varepsilon(\mathbf{r}) |\mathbf{E}_0(\mathbf{r} - 2na\mathbf{x})|^2]\, d^3r}, \tag{2.7}$$

where **y** is the unit direction vector along *y*-direction. Let $u_n(t) = U \exp(2ikna - i\omega_2 t)$ and $v_n(t) = V \exp(2ikna - i\omega_2 t)$, where U and V are the constant amplitudes. By substituting these into Eq. (2.4) and Eq. (2.5), we can obtain

$$U(\omega_2 - \omega_1) + V[\alpha + 2\beta\cos(2ka)] = 0 \tag{2.8}$$

$$V(\omega_2 - \omega_1) + U[\alpha + 2\beta\cos(2ka)] = 0, \tag{2.9}$$

where $\omega_1(k)$ is the dispersion relation of a single PCS-CROW in Eq. (2.3). Therefore, the dispersion relation of the opposite-type PCS-DC can be expressed as

$$\omega_2(k) = \omega_1(k) \pm [\alpha + 2\beta\cos(2ka)], \tag{2.10}$$

where α causes the frequency shift and β leads to the sinusoidal modulation of the dispersion curves. Under the condition $|\beta/\alpha| > 1/2$, these curves will cross at a wave vector $k = [\cos^{-1}(-\alpha/2\beta)]/2a$, where $\alpha + 2\beta\cos(2ka) = 0$.

2-3.2 Alternating-type PCS-DC

On the other hand, in the alternating-type PCS-DC, $u_n(t)$ is the temporal amplitude of the perturbed mode at defect site n of one PCS-CROW, and $v_{n+1/2}(t)$ is the same thing at defect site $n + 1/2$ of another PCS-CROW. Similarly, the coupled equation can be written as

$$i(\partial u_n / \partial t) = (\omega_0 - C_0)\, u_n - \sum_{p=1}^{2} C_p (u_{n+p} + u_{n-p}) \tag{2.11}$$

$$- \alpha(v_{n+1/2} + v_{n-1/2}) - \beta(v_{n+3/2} + v_{n-3/2})$$

$$\mathrm{i}\,(\partial v_{n+1/2}/\partial t) = (\omega_0 - C_0)\,v_{n+1/2} - \sum_{p=1}^{2} C_p\,(v_{n+1/2+p} + v_{n+1/2-p}) \qquad (2.12)$$

$$-\alpha\,(u_n + u_{n+1}) - \beta\,(u_{n+2} + u_{n-1})\,,$$

where α and β are the coupling coefficients of a defect at site n in one PCS-CROW induced by the nearest neighboring (at sites $n \pm 1/2$) and the next-nearest neighboring (at sites $n \pm 3/2$) defects of another PCS-CROW, and are defined as

$$\alpha = \frac{\omega_0 \int_{-\infty}^{\infty} \Delta\varepsilon(\mathbf{r})\,\mathbf{E}_0(\mathbf{r} - 2na\mathbf{x}) \cdot \mathbf{E}_0(\mathbf{r} - 2(n \pm 1/2)a\mathbf{x} + D\mathbf{y})\,\mathrm{d}^3r}{\int_{-\infty}^{\infty} [\mu_0\,|\mathbf{H}_0(\mathbf{r} - 2na\mathbf{x})|^2 + \varepsilon(\mathbf{r})\,|\mathbf{E}_0(\mathbf{r} - 2na\mathbf{x})|^2]\,\mathrm{d}^3r} \qquad (2.13)$$

$$\beta = \frac{\omega_0 \int_{-\infty}^{\infty} \Delta\varepsilon(\mathbf{r})\,\mathbf{E}_0(\mathbf{r} - 2na\mathbf{x}) \cdot \mathbf{E}_0(\mathbf{r} - 2(n \pm 3/2)a\mathbf{x} + D\mathbf{y})\,\mathrm{d}^3r}{\int_{-\infty}^{\infty} [\mu_0\,|\mathbf{H}_0(\mathbf{r} - 2na\mathbf{x})|^2 + \varepsilon(\mathbf{r})\,|\mathbf{E}_0(\mathbf{r} - 2na\mathbf{x})|^2]\,\mathrm{d}^3r}\,. \qquad (2.14)$$

Let $u_n(t) = U \exp(2ikna - i\omega_2 t)$ and $v_{n+1/2}(t) = V \exp[2ik(n + 1/2)a - i\omega_2 t]$, where U and V are the constant amplitudes, and substituting these into Eq. (2.11) and Eq. (2.12). We can gain

$$U\,(\omega_2 - \omega_1) + 2V\,[\alpha\cos(ka) + \beta\cos(3ka)] = 0 \qquad (2.15)$$

$$V\,(\omega_2 - \omega_1) + 2U\,[\alpha\cos(ka) + \beta\cos(3ka)] = 0\,, \qquad (2.16)$$

and the dispersion relation of the alternating-type PCS-DC can be derived as

$$\omega_2(k) = \omega_1(k) \pm 2[\alpha\cos(ka) + \beta\cos(3ka)]\,, \qquad (2.17)$$

where both α and β lead to the sinusoidal modulation of the dispersion curves, which will cross at a wavevector $k = \cos^{-1}[\sqrt{3 - (\alpha/\beta)}/2]/a$ under the condition $|\beta/\alpha| > 1/3$.

Chapter 3 Simulation Results and Discussion

3-1 PWEM of the three-dimensional PC structures

When simulating the PC structures by the PWEM, we must select a finite super cell to repeat and to form the whole infinite structure. However, when a specific super cell is chosen, we find that there will exist some guiding modes different from the defect modes in the PBG, and the corresponding electric field distribution of these modes is not localized in the defects but extended over the whole cell. Additionally, frequencies of these modes are highly influenced by the size of the super cell, so that can be determined as the artifact caused by the boundary conditions of the finite cell. We call these fake modes as the boundary guiding modes (BGMs).

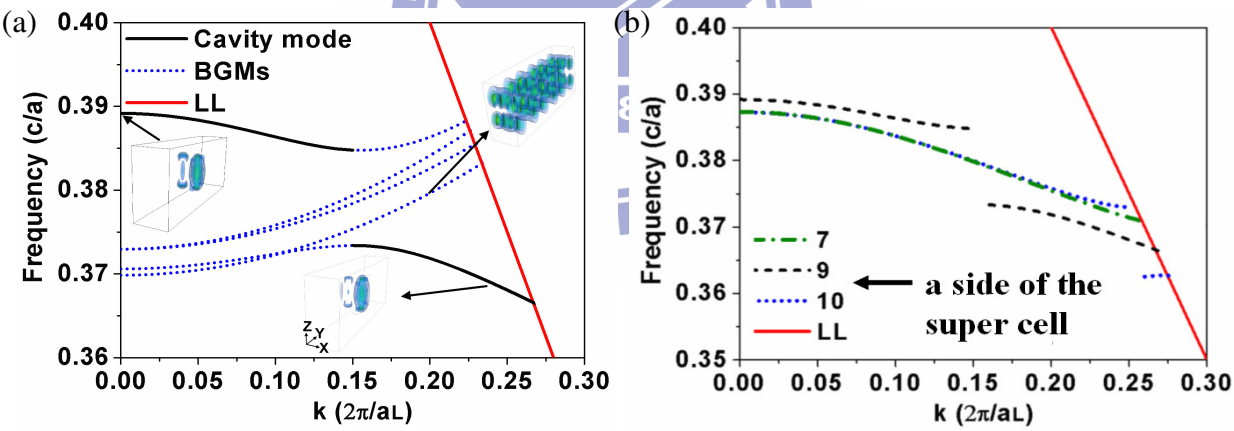

Fig. 3.1 Dispersion curves and corresponding mode distribution of a single dielectric-rod PCS-CROW (a) simulated by the super cell of size 2*a* * 9*a* * 4*a* and (b) by varying the size of the super cell from 7*a* to 10*a* in *y*-direction.

For the PCS-CROW structures, the existence of the BGMs will interfere with the defect modes in the PBG, and cause the discontinuities or jumping to the dispersion curves as in Fig.

3.1(a), which prevent us from obtaining the real values of the defect bands. However, because the BGMs will generally shift to the lower frequencies as the size of the super cell increases, the dispersion relations can be free from these simulation errors by proper choosing the cell boundaries, as shown in Fig. 3.1(b). Additionally, the non-integral size of the boundaries may cause the surface modes, whose field distribution is mainly localized around the interface between the boundaries, and that also can be eliminated by carefully adjusting the simulation cell.

On the other hand, from the PWEM simulation results of the dielectric-rod PCS-CROW and the 2D structures made with the same parameters in Fig. 3.2(a), we find that the dispersion curves of the PCS-CROW nearly parallel shift to the higher frequencies as compared with the 2D structures. It may because the evanescent waves will extend outside the slab, which makes the effective refraction index become lower than the 2D cases. In such cases, the group velocities determined by the slope of the curves are approximately equal. On the other hand, for the air-hole PCS-CROW and corresponding 2D structures in Fig. 3.2(b), their dispersion curves are no longer parallel to each other. In addition, the group velocities of the 2D cases are larger than that in the PCS-CROW because the electric fields are mainly localized in the dielectric connection between the defect holes.

(a)

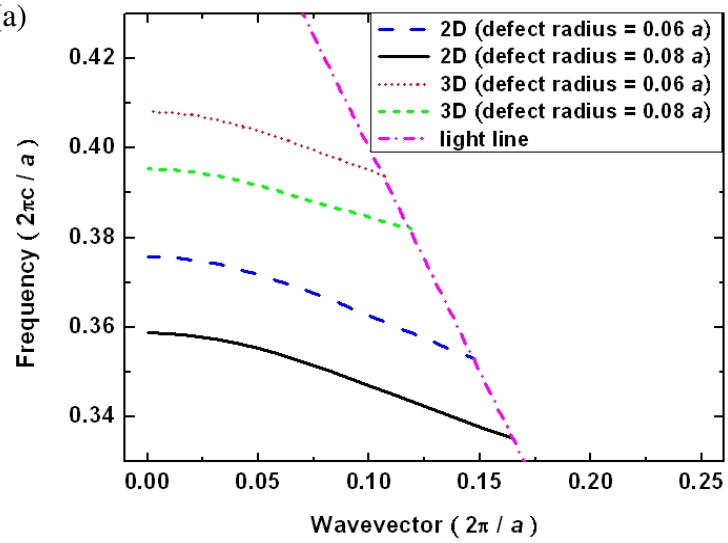

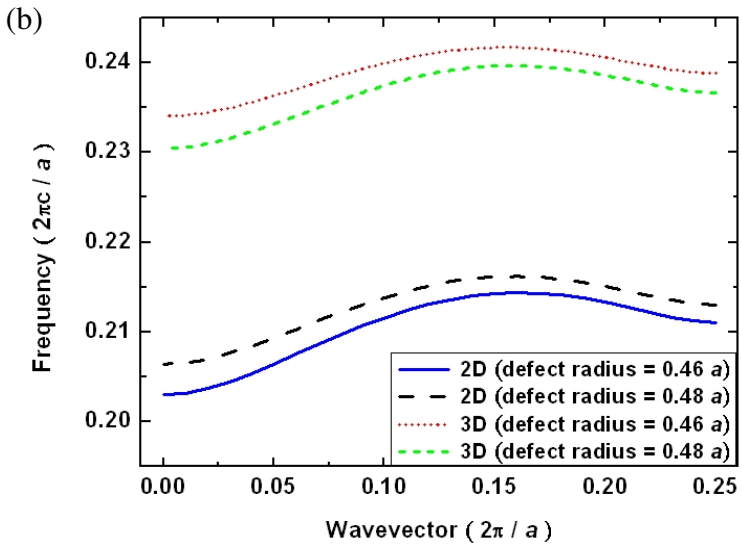

Fig. 3.2 Dispersion relations of a single PCS-CROW and corresponding 2D structures made of (a) dielectric rods in air with a square lattice and (b) air holes in dielectric substrate with a triangular lattice.

3-2 Dielectric-rod structures

In the next sections, in order to examine the validity of the equations derived by the TBT, we first use the PWEM to simulate the eigenfrequency shift and the variation of electric field distribution of a single point defect in the PCS by modifying the defect radius, and the changes of the coupling coefficients in these equations can be obtained. Therefore, the predictions based on the TBT can be verified by comparing with the dispersion relations done by the PWEM. Furthermore, from the dispersion behaviors of the PCS-DCs with different types, we can also discuss their possible applications for photonic devices.

First, we focus on the structures made by a square lattice of dielectric rods in air, as shown in Fig. 2.1(a), Fig. 2.2(a) and Fig. 2.3(a), and the radius, the height and the dielectric constant of the dielectric rods are 0.2a, 2a, 12, respectively, where a is the lattice constant. The chosen refraction index corresponds to the EM waves with 1.75 μm wavelength propagating in the silicon at room temperature, as in Fig. 3.3 [44].

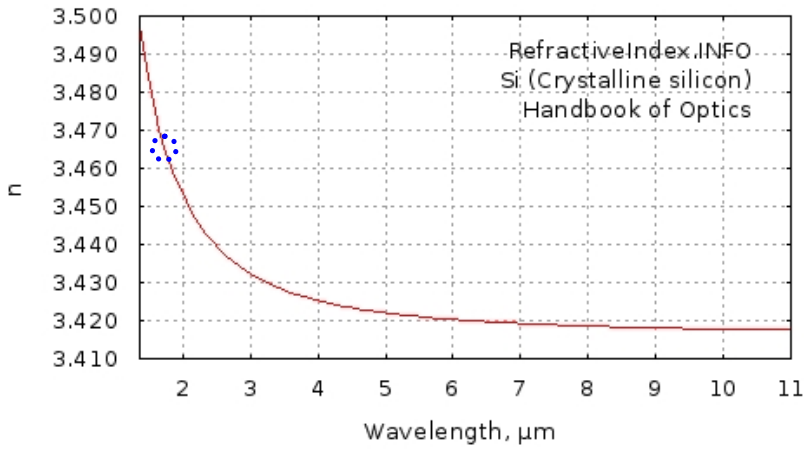

Fig. 3.3 The relationship between the refraction index of silicon and the wavelength of EM waves at room temperature [44], where the blue circle indicates the dielectric constant we use in the simulations.

Additionally, the other parameters are chosen to form a relatively large PBG, which is convenient for observing the behaviors of the defect modes. From the photonic band diagrams of the structure with perfect lattice for different polarization waves, as shown in Fig. 3.4(a) and Fig. 3.4(b), it is clear that the TM-like polarization EM waves (electric fields are mainly parallel to the rod axis) are easier to generate the larger PBG, which localized in the frequency region from 0.333 ($2\pi c/a$) to 0.428 ($2\pi c/a$).

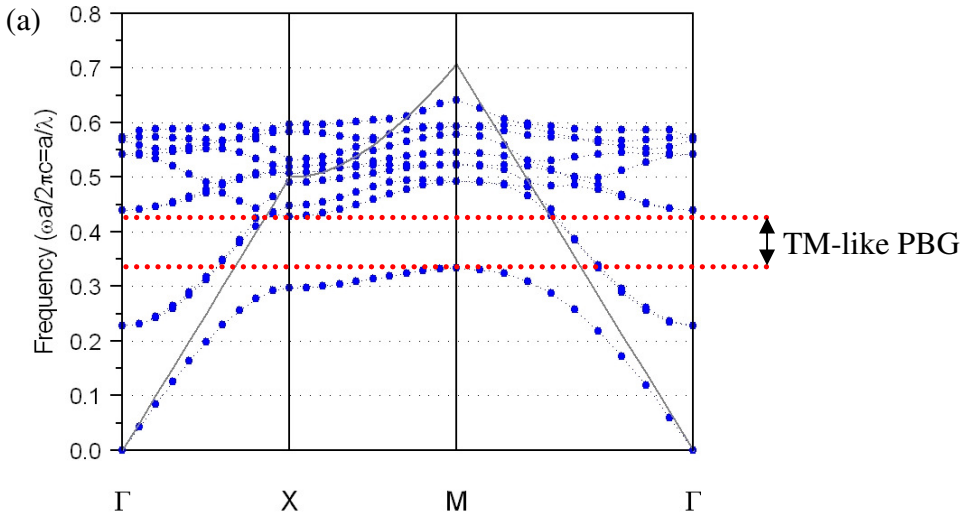

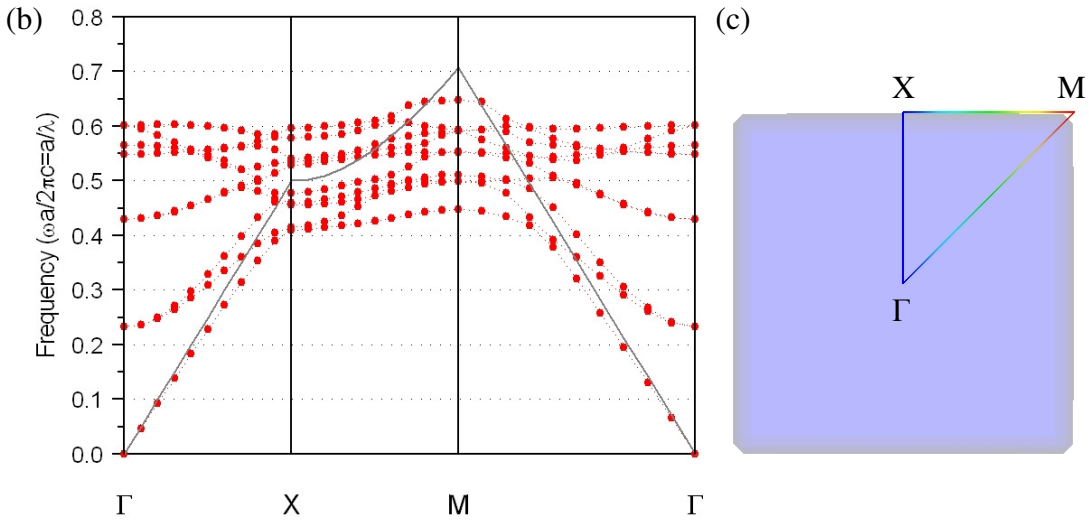

Fig. 3.4 Photonic band diagrams of the perfect dielectric-rod PCS for (a) TM-like and (b) TE-like polarization EM waves, where the gray lines are the light line and the TM-like PBG is marked, and (c) first Brillouin zone of square lattice with irreducible zone for calculation.

3-2.1 Modifying a point defect

Because the EM waves guided in this kind of structures are chosen as the TM-like polarization, the x-component (E_x) and y-component (E_y) of electric field amplitudes are too small to influence the coupling effects between the defects and can be neglected. Therefore, we consider only the electric fields of z-polarization (E_z), and the field distribution of a single point defect simulated by the PWEM is shown in Fig. 3.5, which is mainly localized around the defect rod and has opposite signs when extending to the nearest neighboring rods.

To realize the variation of parameters in the derived equations, we first modify the radius of the defect from $0.06a$ to $0.12a$. As the PWEM simulation result shown in Fig. 3.6, enlarging the defect radius will shift the eigenfrequency ω_0 of a single point defect toward the lower frequencies because of more fields being confined in the defect rod [45] consistent with the results around $X = 0a$ in Fig. 3.7(a).

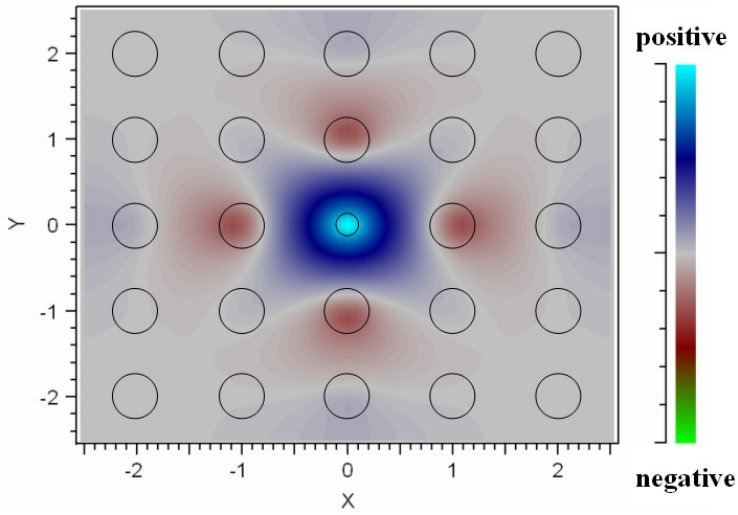

Fig. 3.5 Electric field distribution of *z*-polarization for a point defect localized at the center of the dielectric-rod PCS, and the defect radius is modified as 0.1 *a*.

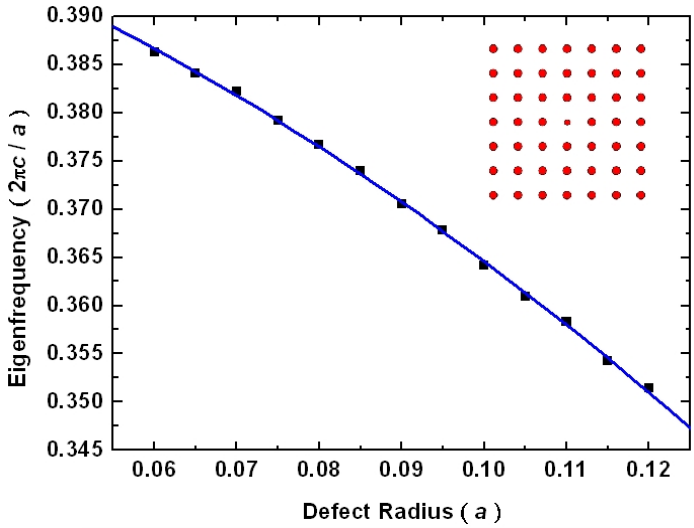

Fig. 3.6 Eigenfrequencies of a point defect in the dielectric-rod PCS.

For observing the influence of this modification on the neighboring regions of the defect , Fig. 3.7(a) and Fig. 3.7(b) show how the electric field distribution varies with the different defect sizes along $y = 0a$ axis and $y = 2a$ axis on the slab plane done by the PWEM. From Fig. 3.7(a), the fields along $y = 0a$ axis are mainly localized on the rods at $X = 0a$ and $X = \pm a$, and will extend to the air region as reducing the defect radius. On the other hand, from Fig. 3.7(b), the fields along $y = 2a$ axis are relatively smaller than that along $y = 0a$ axis, and have no certain trends at different sites when the defect radius varying.

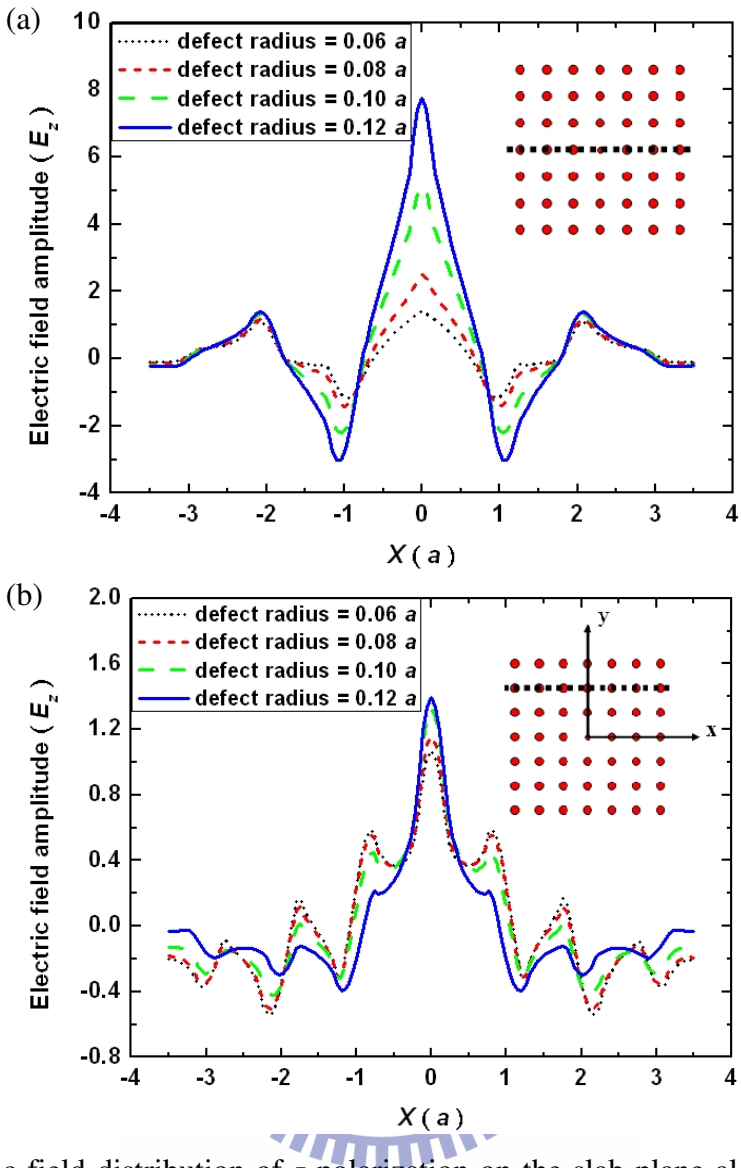

Fig. 3.7 Electric field distribution of z-polarization on the slab plane along (a) $y = 0a$ axis and (b) $y = 2a$ axis of a point defect in the dielectric-rod PCS.

3-2.2 Properties of a single PCS-CROW

As defined in Eq. (2.2), C_1 and C_2 are the nearest neighboring and the next-nearest neighboring coupling coefficients of one point defect in a single PCS-CROW. By observing the electric field amplitudes of z-polarization around $X = 0a$ and $X = 2a$ along the propagation axis ($y = 0a$ axis) on the slab plane as in Fig. 3.7(a), we find that the field in a single point defect has the same sign as it extends to the nearest neighboring defects, i.e. $E_{0z}(\boldsymbol{r} - 2na\boldsymbol{x})$

$E_{0z}(\boldsymbol{r} - 2(n+1)a\boldsymbol{x}) > 0$, and C_1 can be estimated being negative due to the negative $\Delta\varepsilon(\mathbf{r})$ of the air defects, which are created by reducing the effective refraction index. The magnitude of C_1 is proportional to the multiplication of the fields at $X = 0a$ and $X = 2a$ and the eigenfrequency ω_0, and the estimated value (normalized) are plotted in Fig. 3.8. It will increase as the defect radius increases. On the other hand, C_2 is much smaller than C_1 due to the small field amplitude at $X = 4a$ and can be neglected.

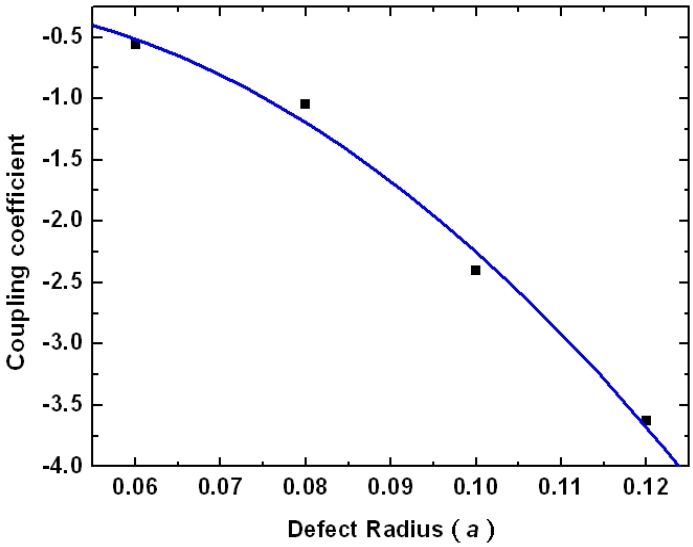

Fig. 3.8 Estimated values (normalized) of the coupling coefficient C_1 in a single dielectric-rod PCS-CROW.

From the dispersion relation derived by the TBT in Eq. (2.3), we know that the frequency shift of curves is primarily dominated by the eigenfrequency ω_0 and the cosine modulation is mainly caused by the coupling coefficient C_1. Therefore, the dispersion curves should move toward the lower frequency by increasing the defect radius because of the decrease of the eigenfrequency ω_0 as the PWEM simulation result in Fig. 3.9. In addition, because the coupling coefficient C_1 is of negative value, the curves will decrease at the higher value of wavevector, which is caused by the decrease of the term $C_1 \cos(2ka)$.

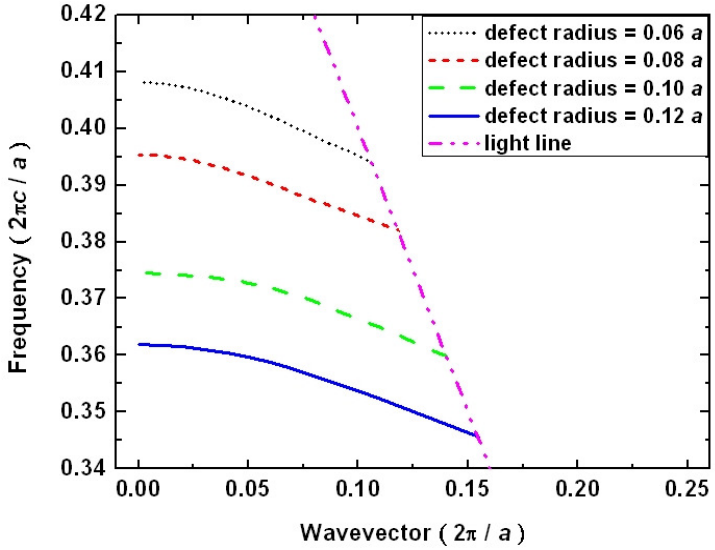

Fig. 3.9 Dispersion curves of a single dielectric-rod PCS-CROW.

3-2.3 Properties of the opposite-type PCS-DCs

Similarly, for the opposite-type PCS-DCs, the defined nearest neighboring coupling coefficient α and the next-nearest neighboring coupling coefficient β can be estimated from the electric field distribution of z-polarization along $y = 2a$ axis on the slab plane as in Fig. 3.7(b). According to Eq. (2.6) and Eq. (2.7), we know that α dominated by the fields around $X = 0a$ is much larger than β dominated by the fields around $X = 2a$ and they possess the opposite signs. The values and the ratio of these two coefficients are plotted in Fig. 3.10(a) and Fig. 3.10(b).

Therefore, from the derived Eq. (2.10), the dispersion curves never have a crossing point due to $|\beta/\alpha| < 1/2$, and the frequency difference between the two curves is nearly a constant for all wavevectors, which is dominated by the term $\alpha + 2\beta\cos(2ka)$. As expected, these predicted trends are consistent with the simulation result by the PWEM in Fig. 3.11. Additionally, the frequency shift of the dispersion curves by varying the defect radius and the decrease of them at the larger wavevector are caused by the frequency $\omega_1(k)$ of a single PCS-CROW as mentioned above.

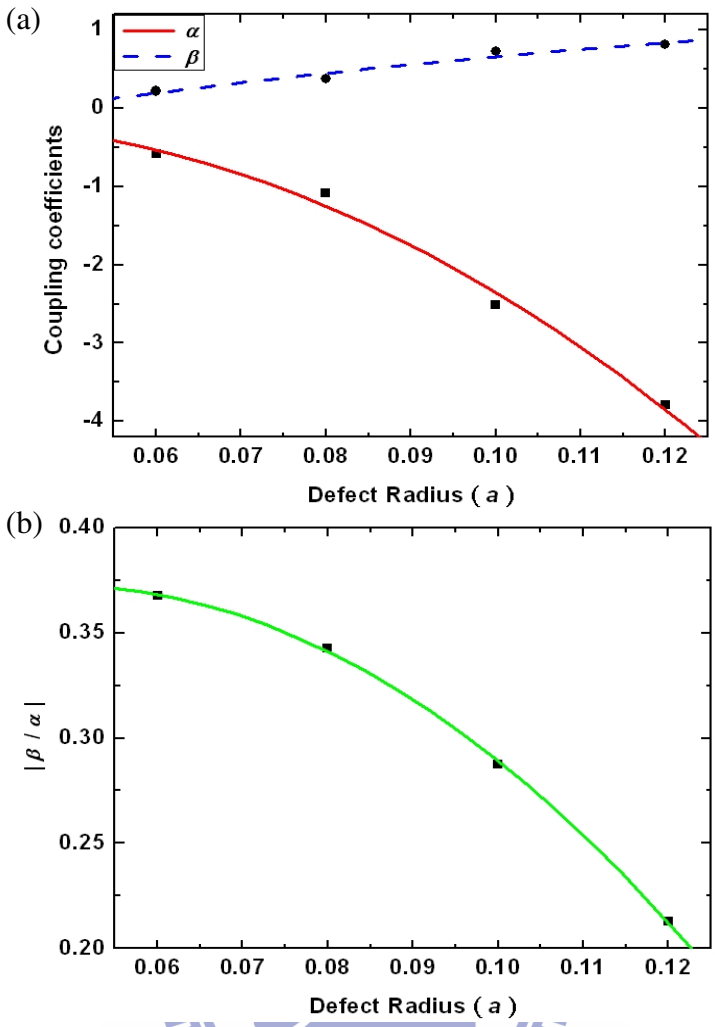

Fig. 3.10 (a) Estimated values (normalized) of the coupling coefficients α and β in the opposite-type dielectric-rod PCS-DCs, and (b) the ratio $|\beta/\alpha|$ for the crossing of curves.

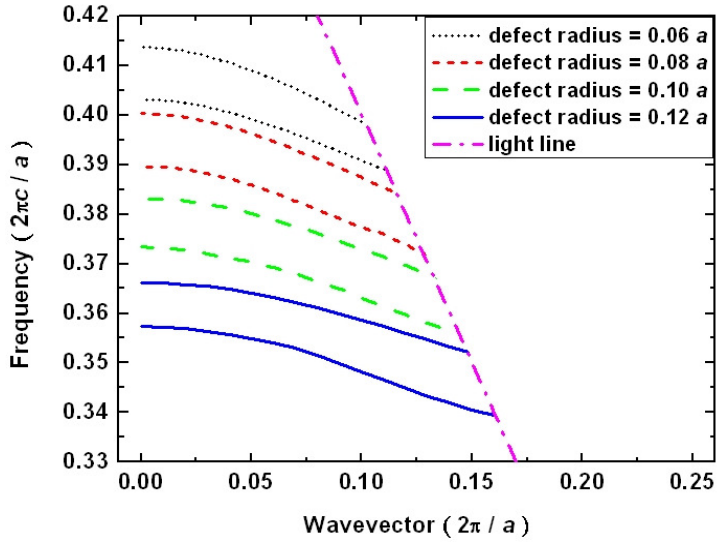

Fig. 3.11 Dispersion curves of the opposite-type dielectric-rod PCS-DCs.

3-2.4 Properties of the alternating-type PCS-DCs

On the other hand, we can analyze the alternating-type PCS-DCs by similar methods. From the electric field distribution of z-polarization along $y = 2a$ axis on the slab plane as in Fig. 3.7(b), the coupling coefficients α dominated by the fields around $X = 1a$ and β dominated by the fields around $X = 3a$ can be obtained by Eq. (2.13) and Eq. (2.14). Owing to the longer distance between the coupling defects, the magnitude of α is much smaller than that in the opposite-type PCS-DCs. Additionally, these two coefficients possess the opposite sign, and the ratio $|\beta/\alpha|$ increases as the defect radius increases because of the decreasing of α, as plotted in Fig. 3.12(a) and Fig. 3.12(b).

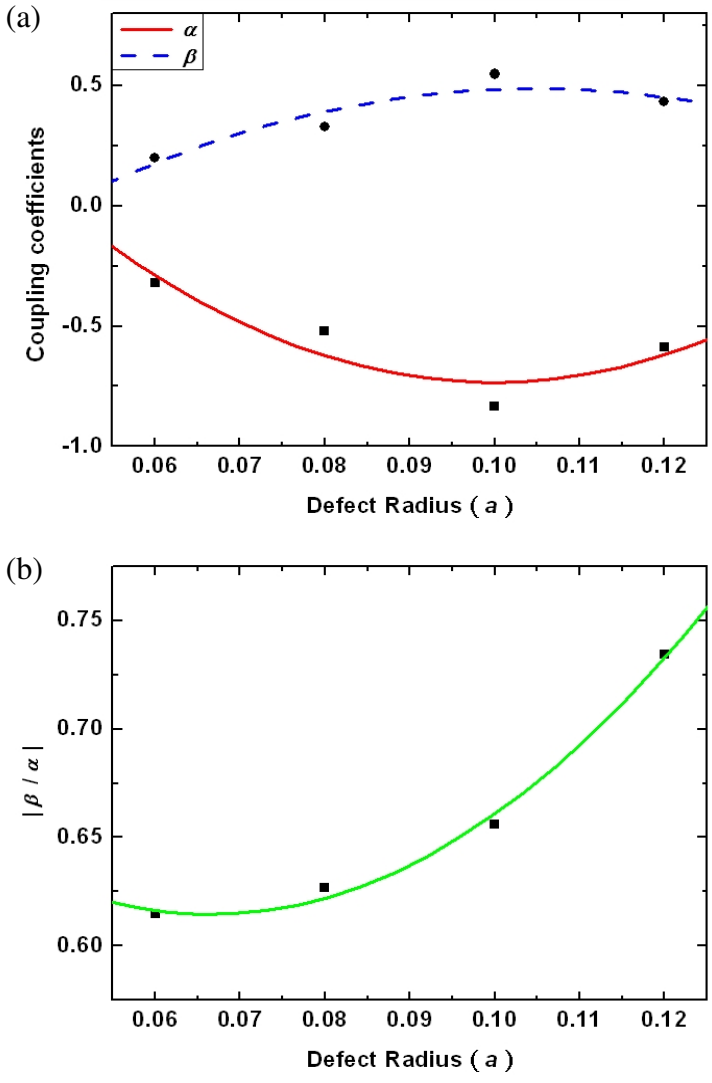

Fig. 3.12 (a) Estimated values (normalized) of the coupling coefficients α and β in the alternating-type dielectric-rod PCS-DCs, and (b) the ratio $|\beta/\alpha|$ for the crossing of curves.

Therefore, from the derived Eq. (2.17), as the condition $|\beta/\alpha| > 1/3$ is reached, all the dispersion curves should have a crossing point, and this decoupling point will shift to the smaller wavevectors $k = \cos^{-1}[\sqrt{3 - (\alpha / \beta)} / 2] / a$ by increasing the defect radius, which is caused by the increasing of the ratio $|\beta/\alpha|$. At this point, the waves propagating in one PCS-CROW will not couple into another. These discussed features are almost consistent with the simulation results done by the PWEM in Fig. 3.13. The absence of the decoupling point of the curves for the structure with defect radius 0.06a may be caused by the crossing above the light line.

Additionally, because α and β both lead to the sinusoidal modulation of the dispersion curves, two decoupling points may exist in the 2D simulation results. However, in the 3D simulations, one of these points is generally localized above the light line in the first Brillouin zone where the electric fields can not be confined in the PCS, so we focus on only one decoupling point of the propagation modes.

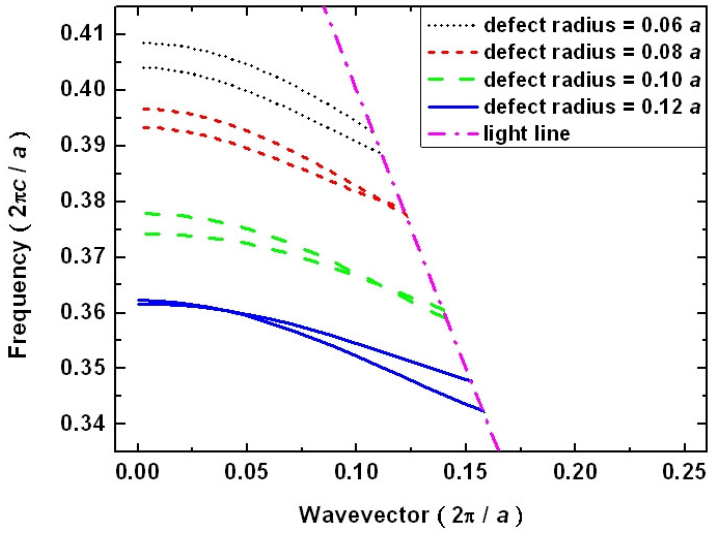

Fig. 3.13 Dispersion curves of the alternating-type dielectric-rod PCS-DCs.

3-3 Air-hole structures

Second, we consider the structures made by a triangular lattice of air holes in dielectric slab, as shown in Fig. 2.1(b), Fig. 2.2(b) and Fig. 2.3(b), and the radius of the holes, the height and the dielectric constant of the slab are 0.3*a*, *a*, 12, respectively. From the photonic band diagrams of the structure with perfect lattice in Fig. 3.14(a) and Fig. 3.14(b), it is clear that the TE-like polarization waves (electric fields are manly parallel to the slab plane) are easier to form the PBG, which localized in the frequency region from 0.233 ($2\pi c/a$) to 0.307 ($2\pi c/a$).

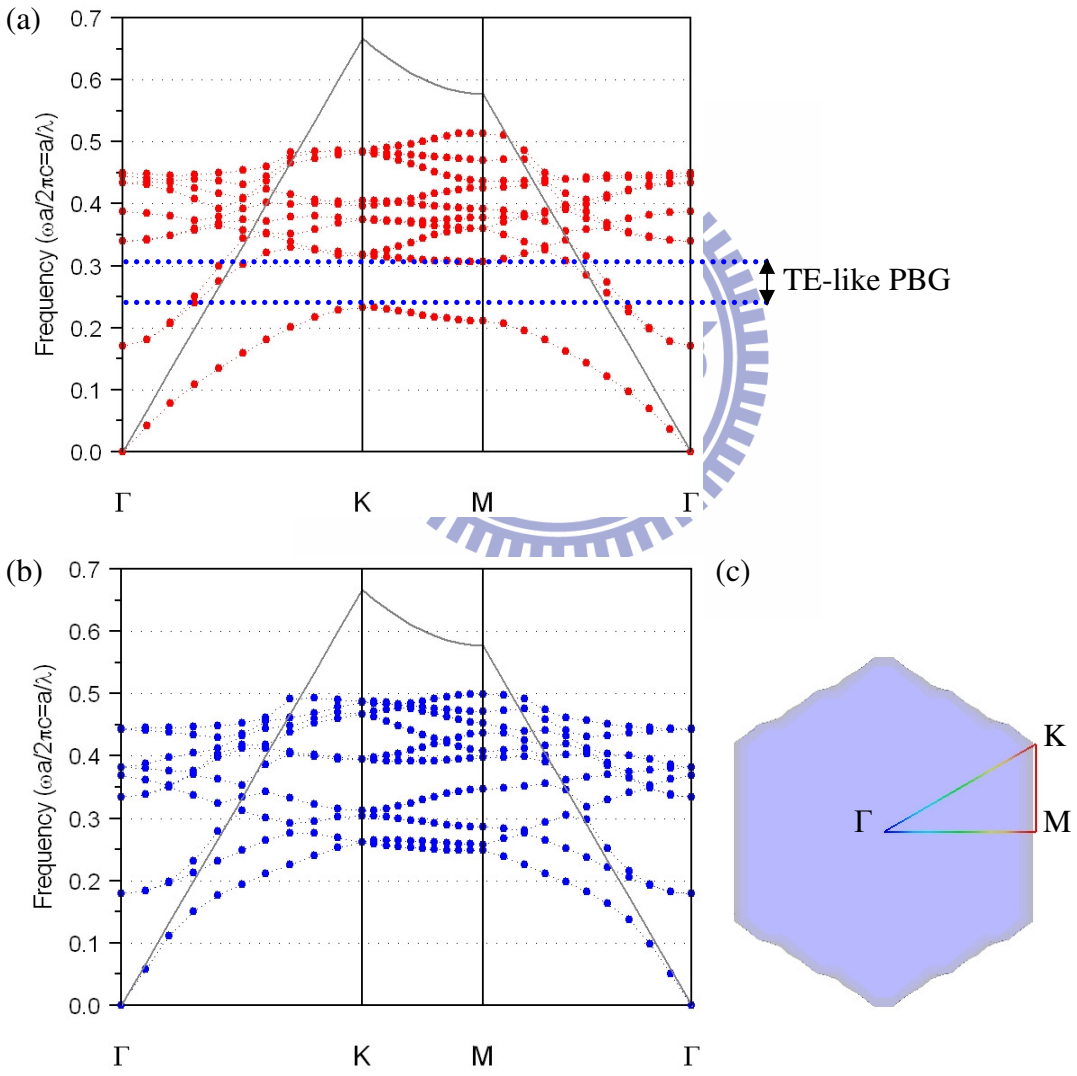

Fig. 3.14 Photonic band diagram of the perfect air-hole PCS for (a) TE-like and (b) TM-like polarization EM waves, and (c) first Brillouin zone of triangular lattice with irreducible zone.

3-3.1 Modifying a point defect

Owing to the TE-like polarization of the EM waves propagating in these structures, the coupling effects contributed by the z-component (E_z) of electric field amplitudes are much smaller than that by transverse fields and can be ignored. Therefore, only the electric fields of x-polarization (E_x) and y-polarization (E_y) should be taken into consideration, and the distribution of field intensity of a single point defect hole simulated by the PWEM is plotted in Fig. 3.15, which is mainly localized at the dielectric connections around the defect hole and the neighboring air holes. In this case, the contribution of E_x and E_y to the coupling coefficients should be discussed individually.

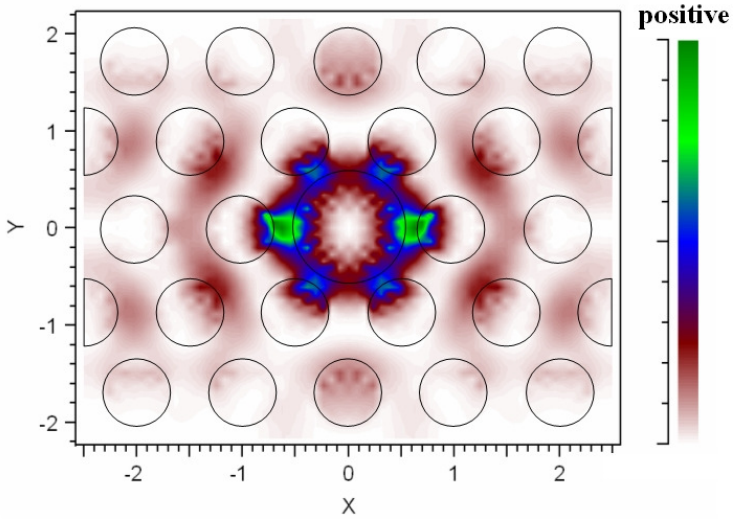

Fig. 3.15 Intensity distribution of the transverse-polarized electric fields for a point defect localized at the center of the air-hole PCS, and the defect radius is modified as 0.5 a.

To obtain the variation of the defined parameters, we modify the radius of the defect hole from 0.44a to 0.50a. As the PWEM simulation result shown in Fig. 3.16, enlarging the defect radius will cause the blueshift to the eigenfrequency ω_0 of a single point defect due to the less concentration of electric fields in the defect hole [45].

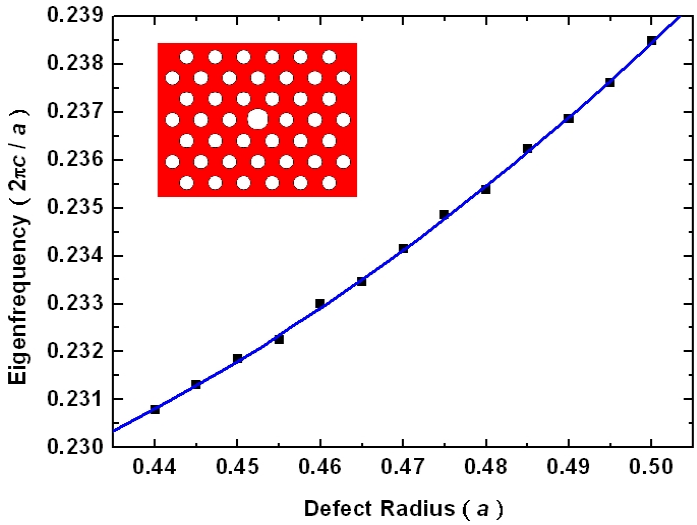

Fig. 3.16 Eigenfrequencies of a point defect in the air-hole PCS.

In order to realize the influence of this modification on the neighboring regions of the defect, Fig. 3.17(a) and Fig. 3.17(b) show the electric field distribution of *x*-polarization varying with the different defect sizes along $y = 0a$ axis and $y = 2a$ axis on the slab plane by the PWEM, and Fig. 3.17(c) and Fig. 3.17(d) are the *y*-polarization electric field distribution under the same conditions. Different from the dielectric-rod structures, the fields at defect sites are almost unchanged by changing the defect radius, which can be explained as the electric fields in the air-hole structures are mainly localized at the connections between holes.

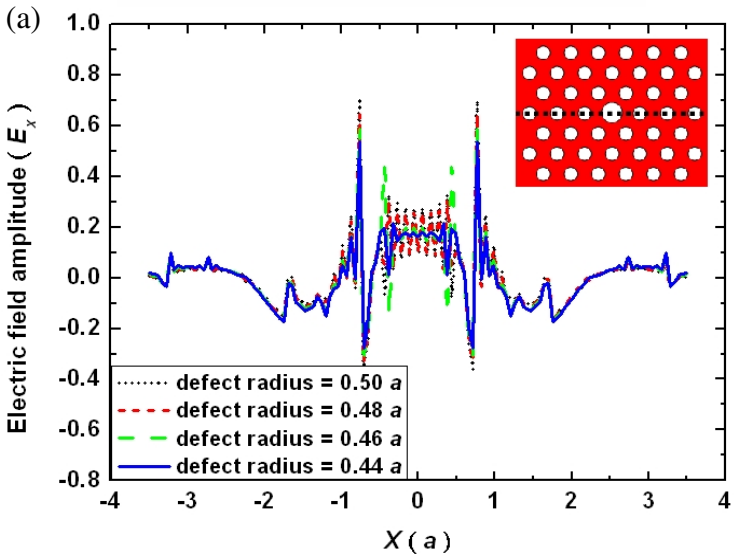

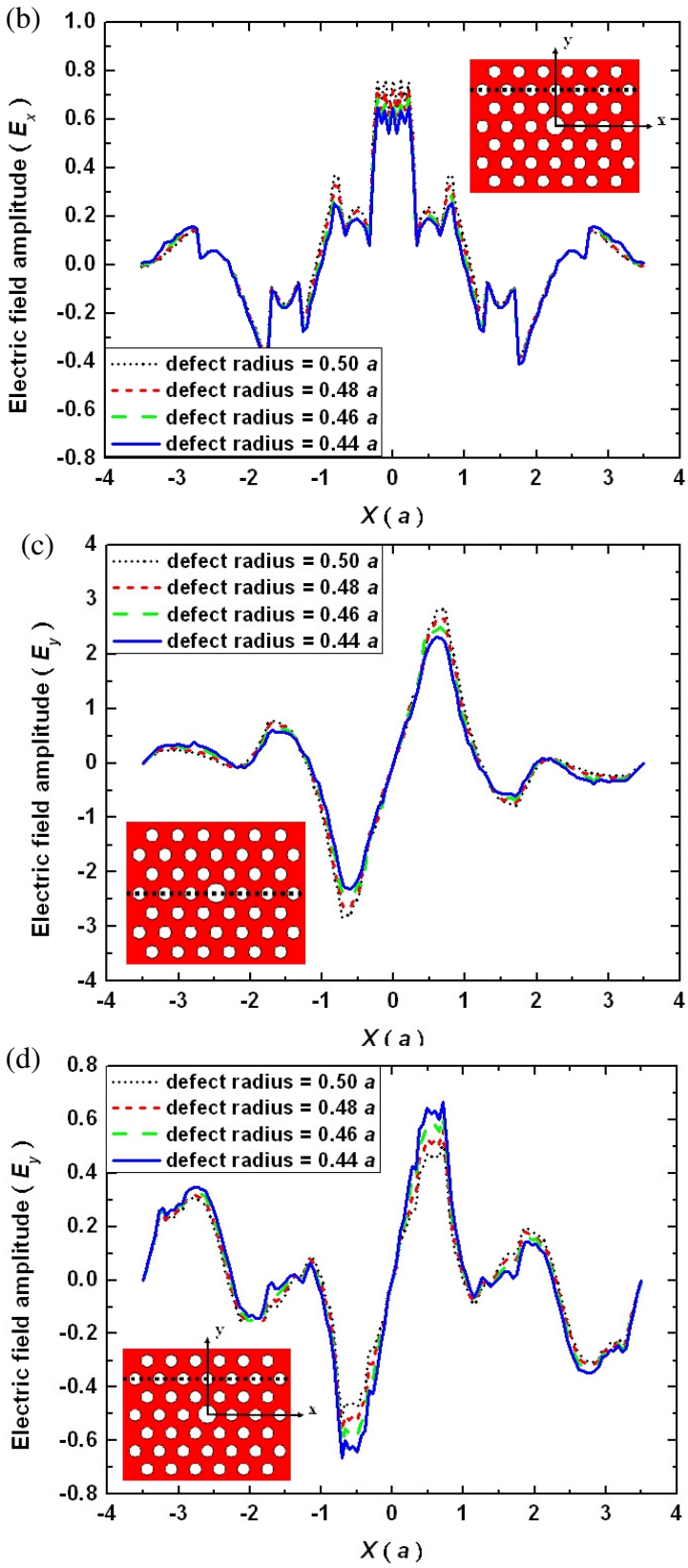

Fig. 3.17 Electric field distribution of *x*-polarization on the slab plane along (a) $y = 0a$ axis and (b) $y = 2a$ axis, and of *y*-polarization along (c) $y = 0a$ axis and (d) $y = 2a$ axis of a single point defect in the air-hole PCS.

3-3.2 Properties of a single PCS-CROW

Considering a single PCS-CROW, C_1 and C_2 are the nearest neighboring and the next-nearest neighboring coupling coefficients of a point defect as defined in Eq. (2.2). From Fig. 3.17(a), we find that E_x around $X = 0a$ and $X = 2a$ along $y = 0a$ axis have the opposite signs and can be slightly influenced by the defect radius. Furthermore, E_x around $X = 4a$ is relatively small and nearly unchanged. Therefore, as in Fig. 3.18(a), when the defect radius increases, C_1 of E_x can be estimated being positive and slightly decreases, and C_2 of E_x remains unaffected. On the other hand, from Fig. 3.17(c), E_y around $X = 0a$, $2a$ and $4a$ are much smaller than E_x, so C_1 and C_2 of E_y are too small to be taken into consideration. These coefficients of E_y are about two orders of magnitude smaller than that of E_x as in Fig. 3.18(b).

From the dispersion relation derived by the TBT in Eq. (2.3), we know that the frequency shift of curves is primarily dominated by the eigenfrequency ω_0 and the cosine modulation is mainly caused by the coupling coefficient C_1 and C_2 of the E_x. According to the PWEM simulation results in Fig. 3.19, the curves will increase and then decrease as the wavevector becoming larger due to the cosine modulation caused by the terms $C_1 \cos(2ka)$ and $C_2 \cos(4ka)$. In addition, the curves just shift to the higher frequency by enlarging the defect holes because of the increase of the eigenfrequency ω_0.

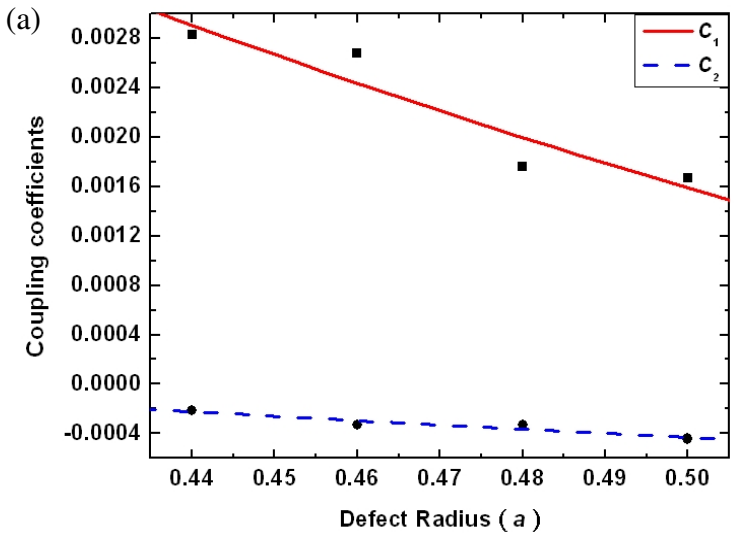

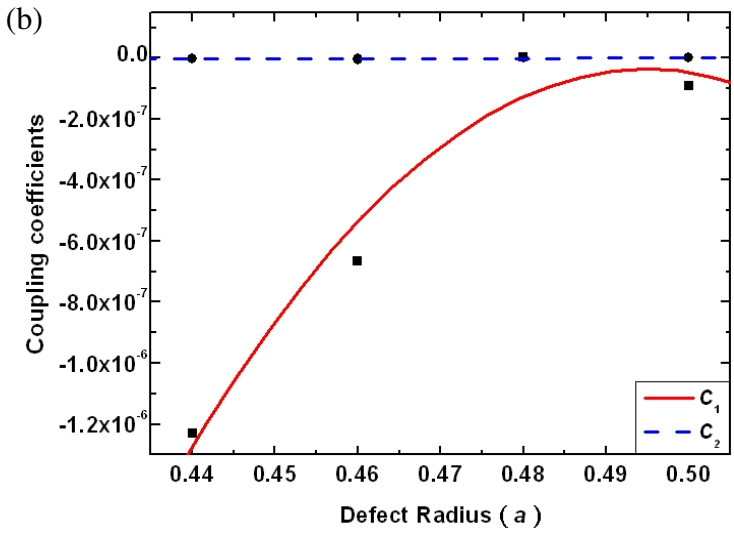

Fig. 3.18 Estimated values (normalized) of the coupling coefficient C_1 and C_2 of (a) E_x and (b) E_y in a single air-hole PCS-CROW.

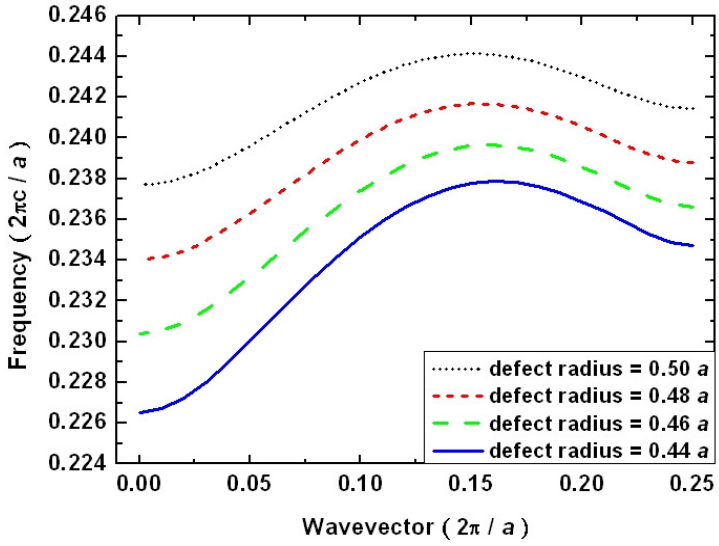

Fig. 3.19 Dispersion curves of a single air-hole PCS-CROW.

3-3.3 Properties of the opposite-type PCS-DCs

Similarly, for the opposite-type PCS-DCs, the nearest neighboring coupling coefficient α and the next-nearest neighboring coupling coefficient β can be discussed from E_x and E_y distribution along $y = 2a$ axis as in Fig. 3.17(b) and Fig. 3.17(d). Additionally, the fields are almost independent from the size of the defects as in a single PCS-CROW. Based on Eq.

(2.6) and Eq. (2.7), the amount of coupling coefficients can be expressed just as the combination of the contribution from the fields with different polarization. From E_x in Fig. 3.17(b), we find that the magnitude of α contributed by the fields around $X = 0a$ is about twice of β contributed by the fields around $X = 2a$ and have the opposite signs. On the other hand, from E_y in Fig. 3.17(d), the α is almost zero and the magnitude of β is smaller than that of E_x. The values of these coupling coefficients and the total ratio between them are plotted in Fig. 3.20(a) and Fig. 3.20(b).

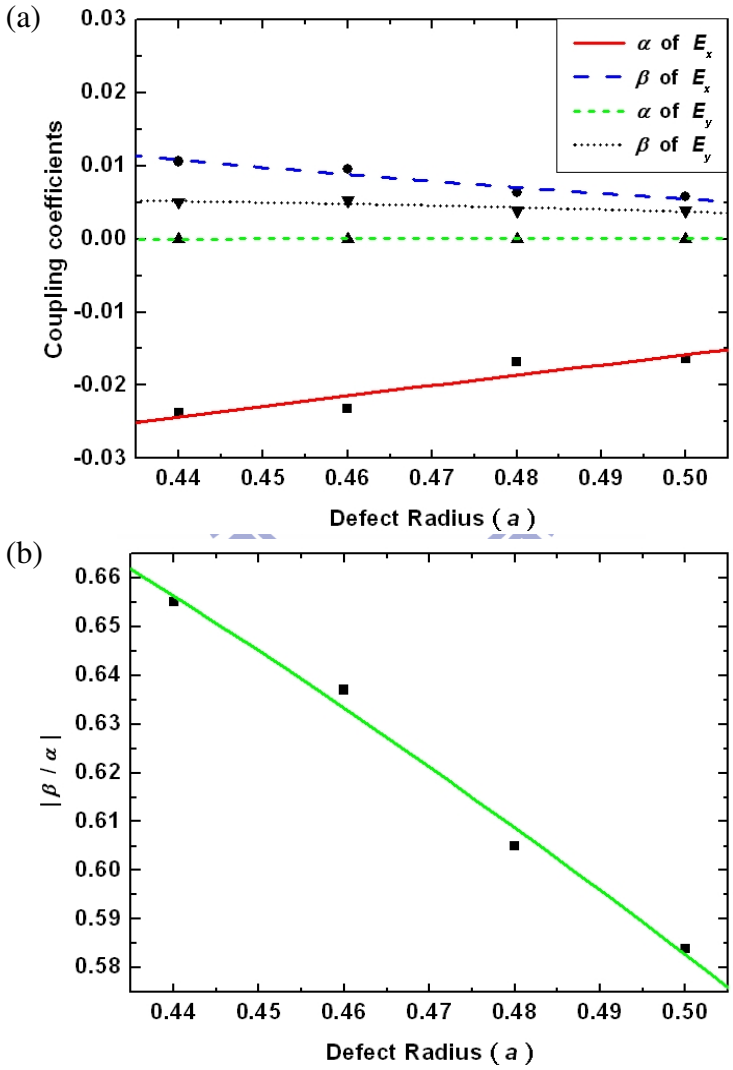

Fig. 3.20 (a) Estimated values (normalized) of the coupling coefficients α and β of E_x and E_y in the opposite-type air-hole PCS-DCs, and (b) the ratio $|\beta/\alpha|$ for the crossing of curves.

Therefore, from the derived Eq. (2.10), we know that all the dispersion relations will have a decoupling point under the condition $|\beta/\alpha| > 1/2$, and the wavevector position of which is nearly a constant, which is caused by the small influence of the defect size on the field distribution. Furthermore, due to the opposite sign of the coefficients α and β, the frequency difference between the splitting curves increases as the wavevector increases, which is dominated by the term $\alpha + 2\beta\cos(2ka)$, and reaches the maximum value at the edge of the first Brillouin zone. Additionally, the frequency shift and sinusoidal modulation of curves with various defect radii is caused by the variation of $\omega_1(k)$ as mentioned above. These predicted trends are consistent with the simulation results done by the PWEM in Fig. 3.21.

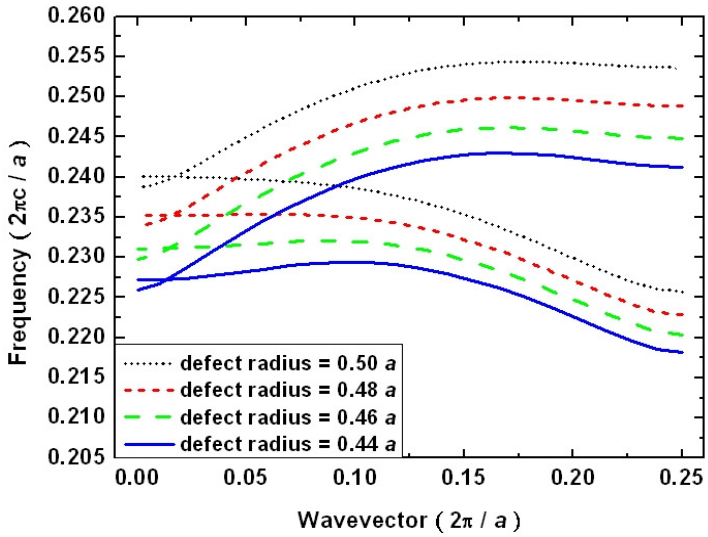

Fig. 3.21 Dispersion curves of the opposite-type air-hole PCS-DCs.

3-3.4 Properties of the alternating-type PCS-DCs

On the other hand, in the alternating-type PCS-DCs, we can discuss in the same way by inspecting E_x and E_y distribution along $y = 2a$ axis in Fig. 3.17(b) and Fig. 3.17(d), and the defined coupling coefficients α contributed by the fields around $X = 1a$ and β contributed by the fields around $X = 3a$ can be obtained from Eq. (2.13) and Eq. (2.14). For both E_x and E_y, α and β are small and almost unaffected by the defect radius, shown in Fig. 3.22(a).

However, the total ratio $|\beta/\alpha|$ can be modified as in Fig. 3.22(b), which decreases as the defect radius increases because of the increase of α, that may caused by the small value of α as the denominator.

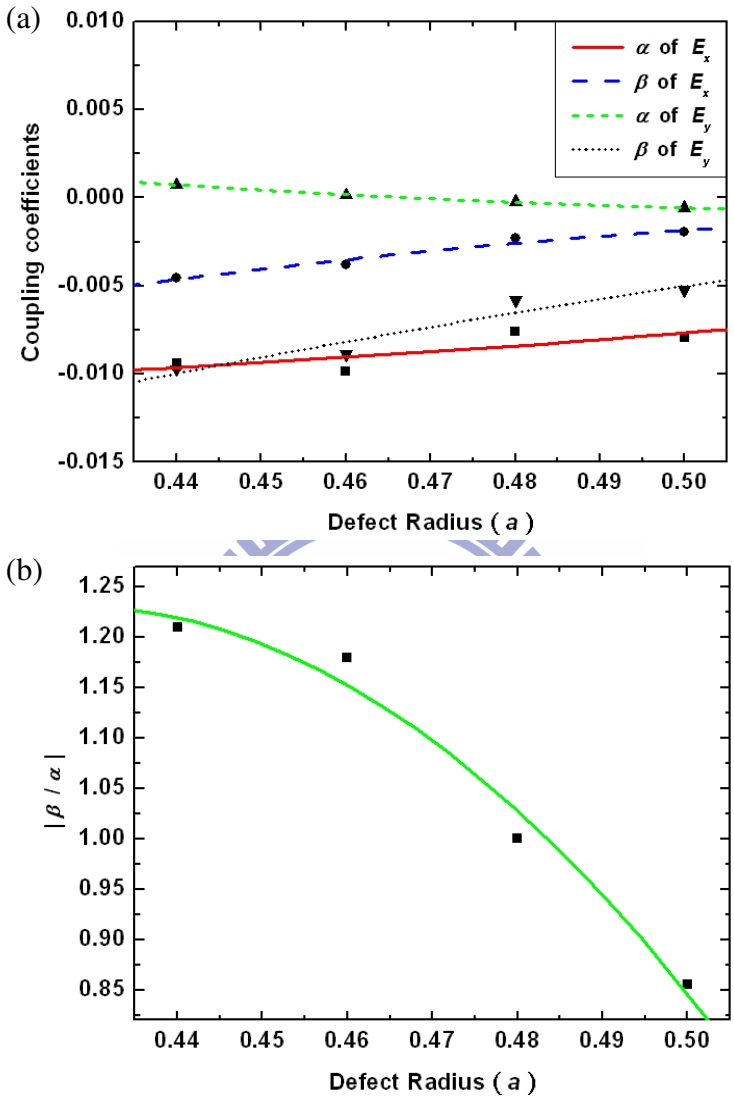

Fig. 3.22 (a) Estimated values (normalized) of the coupling coefficients α and β of E_x and E_y in the alternating-type air-hole PCS-DCs, and (b) the ratio $|\beta/\alpha|$ for the crossing of curves.

Consequently, according to the terms of cosine modulation $\alpha\cos(ka) + \beta\cos(3ka)$ in Eq. (2.17), the dispersion relation would have two crossing points under the condition $|\beta/\alpha| > 1/3$, and one of which is at the edge of the first Brillouin zone. As plotted in Fig. 3.23, the wavevector positions of the decoupling points are nearly constants as in the opposite-type

PCS-DCs, but will slightly shift to the larger values as the defect radius increases. Additionally, we find that the frequency difference between the two splitting curves increases and then decreases as the wavevector shifting to the larger values because α and β both positive and lead to the sinusoidal modulation of the dispersion curves.

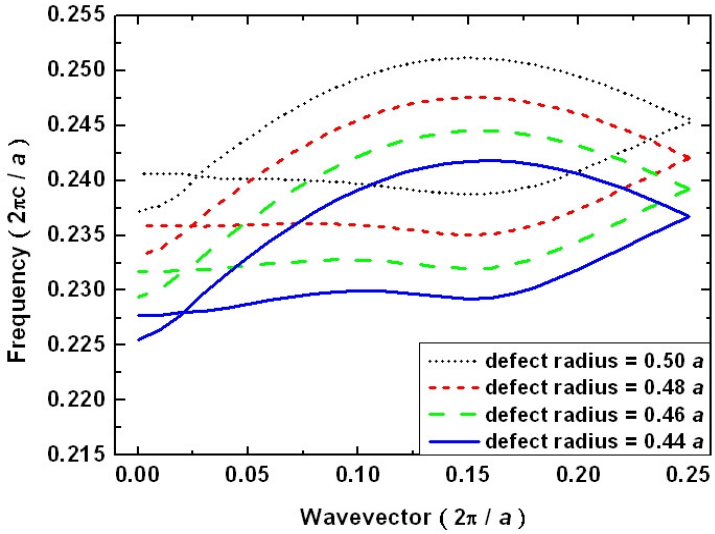

Fig. 3.23 Dispersion curves of the alternating-type air-hole PCS-DCs.

3-4 Applications of the PCS-DCs

We have discussed the dispersion behaviors of the dielectric-rod and air-hole PCS-DCs with different types, and find an effective modal to provide the design concepts. For the opposite-type dielectric-rod PCS-DCs, the frequency difference between the dispersion curves is nearly a constant for all wavevectors, as shown in Fig. 3.11, which means that the coupling length of the device is almost unchanged for the waves with a certain range of frequencies. As expressed in Fig. 3.24(a), this feature can be used to separate the waves with frequencies $\Delta\omega_2$ from a broadband optical signal with frequencies $\Delta\omega_1 + \Delta\omega_2$, where $\Delta\omega_2$ is in the frequency range mentioned above. In addition, because the coupling lengths for the separated waves are the same, these waves can keep their relative phases after coupling from one waveguide into another one. Furthermore, for the alternating-type dielectric-rod

PCS-DCs, the position of the decoupling point can be modified by varying the defect radius, as shown in Fig. 3.13. Waves with the frequency corresponding to the decoupling point can stay in one waveguide without coupled into another one. Therefore, we can separate the waves with a certain frequency ω_1 from a wideband optical signal with frequencies $\Delta\omega$ by properly choosing the parameters of the device, as expressed in Fig. 3.24(b). In conclusion, these two structures can be used to form the demultiplexers for different ranges of frequencies, and can provide the slow-light propagation at the small wavevectors.

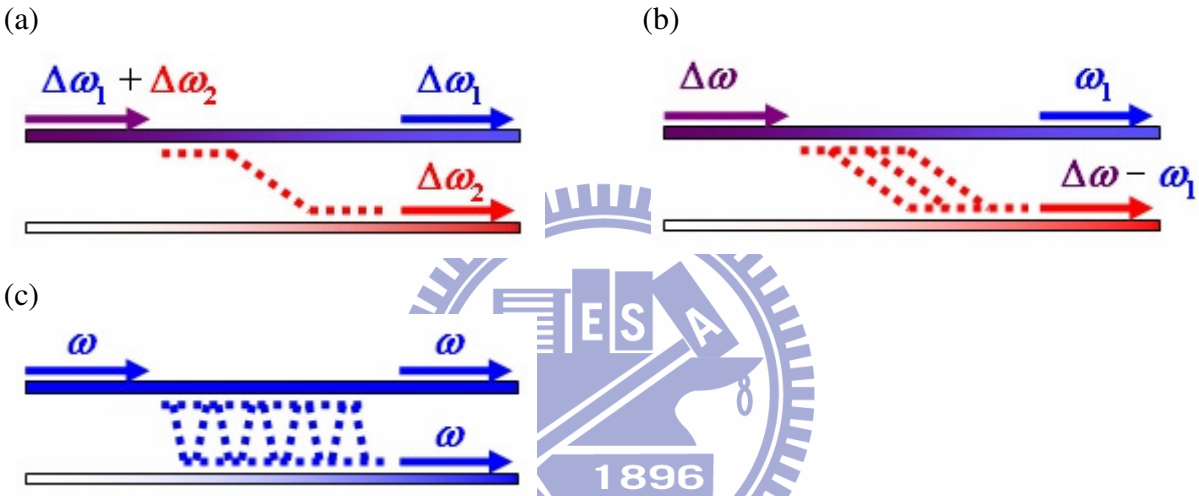

Fig. 3.24 Applications for the (a) opposite-type and (b) alternating-type dielectric-rod PCS-DCs, and for the (c) opposite-type air-hole PCS-DCs.

For the air-hole PCS-DCs, the wavevector position of the decoupling point is almost fixed under different defect radii, so this kinds of structures are hard to be used to separate waves. However, for the opposite-type PCS-DCs, the dispersion curves can support only one even mode or one odd mode at a certain frequency, as shown in Fig. 3.21, which means that the output waves of the two waveguides will have the same phase or a phase difference π. As expressed in Fig. 3.24(c), the incident waves will be separated with a specific phase difference (zero or π) in the two waveguides after propagating a sufficient long distance, and

can be used to form the beam splitters. In addition, that can provide the slow-light propagation near the edge of first Brillouin zone. On the other hand, for the alternating-type PCS-DCs, because the dispersion relations show the multi-mode propagation, this structure is hard to be used due to the complexity of designing.

Chapter 4 Conclusion and Perspectives

4-1 Conclusion

By applying the extended tight-binding theory (TBT), which includes the coupling effects up to the next-nearest neighboring defects, we successfully derive the analytical equations used to describe the dispersion behaviors and the mode distribution of the symmetric directional couplers (DCs) based on the coupled resonant optical waveguides (CROWs) in the photonic crystal slab (PCS). We choose the structures created by a square lattice of dielectric rods in air and a triangular lattice of air holes in a dielectric slab, and the defects are formed by reducing the effective refraction index, which means to reduce the radius of dielectric rods or to enlarge the radius of air holes.

Additionally, for the 3D PWEM simulations, there may exist the fake guiding modes called the boundary guiding modes (BGMs) in the photonic bandgap (PBG) due to the finite size of the simulation super cell. These modes can interfere with the defect modes and cause the discontinuities to the dispersion curves. By proper choosing the non-integral times of the lattice constant as the cell boundaries, we can shift the BGMs outward the PBG and the dispersion relation will free from the simulation errors.

In a single PCS-CROW, the eigenfrequency ω_0 of a single point defect will cause the frequency shift to the dispersion curves, and the coupling coefficients C_1 and C_2 lead to the sinusoidal modulation. In the opposite-type PCS-DCs, the nearest neighboring coupling coefficient α causes the splitting and the next-nearest neighboring coupling coefficient β leads to the sinusoidal modulation of the dispersion curves, which will cross at a point under the condition $|\beta/\alpha| > 1/2$. On the other hand, in the alternating-type PCS-DCs, both α and β lead to the sinusoidal modulation to the dispersion relations, and the curves will have a decoupling

point under the condition $|\beta/\alpha| > 1/3$.

In the dielectric-rod structures, the coupling coefficients are dominated by the electric fields parallel to the rod axis (z-polarization) owing to the TM-like polarization propagating waves, and ω_0 will shift toward the lower frequency by increasing the radius of the defect rods. For a single PCS-CROW, C_2 is much smaller than C_1 and can be neglected, and C_1 can be estimated being negative. The dispersion curves of that will move toward the lower frequency by increasing the defect radius, and decrease at the higher values of the wavevector. In addition, for the opposite-type PCS-DCs, we find that α is much larger than β and they possess the opposite sign. Therefore, the dispersion curves never have a crossing point, and the frequency difference between them is nearly a constant for all wavevectors, which can be used to separate the waves with the frequencies in a certain range from a broadband optical signal. On the other hand, for the alternating-type PCS-DCs, the magnitude of α is much smaller than that in the opposite-type PCS-DCs and the ratio $|\beta/\alpha|$ increases as the defect radius increases due to the decrease of α. Consequently, the dispersion curves of the structures with the larger defect rods may have a crossing point, which will shift to the smaller wavevector by increasing the defect radius. At this so-called decoupling point, the EM waves will propagate in one waveguide without leaking to another one, and the coupling length becomes infinite. This feature can be used to separate the waves with a certain frequency from a wideband optical signal by properly choosing the parameters of the device.

On the other hand, in the air-hole structures, the coupling coefficients are dominated by the electric fields parallel to the slab plane (x-polarization and y-polarization) due to the TE-like polarization propagating waves, and the enlarging of defect holes will cause the blueshift to the eigenfrequency ω_0. For a single PCS-CROW, C_1 and C_2 of the y-polarization waves are too small to be taken into consideration, and these coupling coefficient can be just slightly influenced by the defect radius. The dispersion curves of that will increase and then decrease as the wavevector becoming larger due to the cosine modulation, and just shift to the

higher frequency by enlarging the defect radius. For the opposite-type PCS-DCs, we find that the magnitude of α is about twice the magnitude of β and they have the opposite sign, and both of them are nearly independent from the size of defects. Therefore, there exists a decoupling point of all the dispersion relations, and the wavevector position of this point is almost a constant. In addition, the frequency difference between the curves increases at the larger wavevector, and reaches the maximum value at the edge of the first Brillouin zone. Furthermore, because this structure can support only one even mode or one odd mode at a certain frequency, that can be used to form the beam splitters with the slow-light propagation near the zone edge. On the other hand, for the alternating-type PCS-DCs, α and β are small and almost unaffected by the defect radius as in the opposite-type PCS-DCs. Consequently, the dispersion relations also have a decoupling point with a certain wavevector. Moreover, the frequency difference between the curves would increase and then decrease as increasing of the wavevector. However, owing to the multi-mode propagation, this structure is hard to be used due to the complexity of designing. In conclusion, these features discussed by the TBT are confirmed by the PWEM simulations, and this analytical method provide valuable design concepts on the PCS-DCs in integrated photonic circuits, which can be controlled by only few parameters related to the coupling effects.

4-2 Perspectives

In this thesis, we have discussed the coupling effects and dispersion behaviors in different types of PCS-DCs, and the characteristics of the signal couplings in these structures have been obtained. However, we consider only the linear optical effects in these structures. The other advantages of the PCS-DCs as the slow-light propagation and nonlinear interaction are also valuable topics, which can make the DCs become the active optical components. For example, the incident EM waves with different intensities can be separated by the

propagating conditions tuned by nonlinear effects. Therefore, the properties of the nonlinear PCS-DCs should be further investigated as the future works, and the devices can be designed to examine whether this kind of structures have practical values.

References

[1] E. Yablonovitch, "Inhibited Spontaneous Emission in Solid-State Physics and Electronics," Phys. Rev. Lett. **58**, 2059-2062 (1987).

[2] S. John, "Strong Localization of Photons in Certain Disordered Dielectric Superlattices," Phys. Rev. Lett. **58**, 2486-2489 (1987).

[3] A. Imhof, W. L. Vos, R. Sprik, and A. Lagendijk, "Large Dispersive Effects near the Band Edges of Photonic Crystals," Phys. Rev. Lett. **83**, 2942-2945 (1999).

[4] Y. A. Vlasov, M. O'Boyle, H. F. Hamann, and S. J. McNab, "Active control of slow light on a chip with photonic crystal waveguides," Nature **438**, 65-69 (2005).

[5] V. Bykov, "Spontaneous emission in a periodic structure," Sov. Phys. JETP **35**, 269-273 (1972).

[6] J. Q. Xi, M. Ojha, J. L. Plawsky, W. N. Gill, J. K. Kim, and E. F. Schubert, "Internal high-reflectivity omni-directional reflectors," Appl. Phys. Lett. **87**, 031111 (2005).

[7] J. Rosenberg, R. V. Shenoi, S. Krishna, and O. Painter, "Design of plasmonic photonic crystal resonant cavities for polarization sensitive infrared photodetectors," Opt. Express **18**, 3672-3686 (2010).

[8] H. Benisty, C. Weisbuch, D. Labilloy, M. Rattier, C. J. M. Smith, T. F. Krauss, R. M. De La Rue, R. Houdr´e, U. Oesterle, C. Jouanin, and D. Cassagne, "Optical and confinement properties of two-dimensional photonic crystals," J. Lightwave Technol. **17**, 2063-2077 (1999).

[9] A. Mekis, J. C. Chen, I. Kurland, S. Fan, P. R. Villeneuve, and J. D. Joannopoulos, "High Transmission through Sharp Bends in Photonic Crystal Waveguides," Phys. Rev. Lett. **77**, 3787-3790 (1996).

[10] S. G. Johnson, S. Fan, P. R. Villeneuve, and J. D. Joannopoulos, "Guided modes in

photonic crystal slabs," Phys. Rev. B **60**, 5751-5758 (1999).

[11] Y. Tanaka, H. Nakamura, Y. Sugimoto, N. Ikeda, K. Asakawa, and K. Inoue, "Coupling Properties in a 2-D Photonic Crystal Slab Directional Coupler With a Triangular Lattice of Air Holes," IEEE J. Quantum Elect. **41**, 76-84 (2005).

[12] M. F. Lu, S. M. Liao, and Y. T. Huang, "Ultracompact photonic crystal polarization beam splitter based on multimode interference," Appl. Opt. **49**, 724-731 (2010).

[13] A. Yariv, Y. Xu, R. K. Lee, and A. Scherer, "Coupled-resonator optical waveguide : a proposal and analysis," Opt. Lett. **24**, 711-713 (1999).

[14] S. Mookherjea, and A. Yariv, "Coupled Resonator Optical Waveguides," IEEE J. Sel. Top. Quant. **8**, 448-456 (2002).

[15] S. Mookherjea, "Dispersion characteristics of coupled-resonator optical waveguides," Opt. Lett. **30**, 2406-2408 (2005).

[16] K. Hosomi, and T. Katsuyama, "A dispersion compensator using coupled defects in a photonic crystal," IEEE J. Quantum Elect. **38**, 825-829 (2002).

[17] J. B. Khurgin, "Optical buffers based on slow light in electromagnetically induced transparent media and coupled resonator structures : comparative analysis," J. Opt. Soc. Am. B **22**, 1062-1074 (2005).

[18] S. Sandhu, M. L. Povinelli, M. F. Yanik, and S. Fan, "Dynamically tuned coupled-resonator delay lines can be nearly dispersion free," Opt. Lett. **31**, 1985-1987 (2006).

[19] M. S. Moreolo, V. Morra, and G. Cincotti, "Design of photonic crystal delay lines based on enhanced coupled-cavity waveguides," J. Opt. A : Pure Appl. Opt. **10**, 064002 (2008).

[20] S. Mookherjea, D. S. Cohen, and A. Yariv, "Nonlinear dispersion in a coupled-resonator optical waveguide," Opt. Lett. **27**, 933-935 (2002).

[21] S. Mookherjea, and A. Yariv, "Pulse propagation in a coupled resonator optical waveguide to all orders of dispersion," Phys. Rev. E **65**, 056601 (2002).

[22] S. Mookherjea, and A. Yariv, “Optical pulse propagation in the tight-binding approximation,” Opt. Express **9**, 91-96 (2001).

[23] D. N. Christodoulides, and N. K. Efremidis, “Discrete temporal solitons along a chain of nonlinear coupled microcavities embedded in photonic crystals,” Opt. Lett. **27**, 568-570 (2002).

[24] C. H. Huang, J. N. Wu, S. C. Cheng, and W. F. Hsieh, “The evolution of solitons in coupled resonator optical waveguides and photonic-crystal waveguides,” Comput. Phys. Commun. **182**, 232-236 (2011).

[25] I. Neokosmidis, T. Kamalakis, and T. Sphicopoulos, “Optical Delay Lines Based on Soliton Propagation in Photonic Crystal Coupled Resonator Optical Waveguides,” IEEE J. Quantum Elect. **43**, 560-567 (2007).

[26] S. Mookherjea, and A. Yariv, “Optical pulse propagation and holographic storage in a coupled-resonator optical waveguide,” Phys. Rev. E **64**, 066602 (2001).

[27] Y. Xu, R. K. Lee, and A. Yariv, “Propagation and second-harmonic generation of electromagnetic waves in a coupled-resonator optical waveguide,” J. Opt. Soc. Am. B **17**, 387-400 (2000).

[28] S. Mookherjea, and A. Yariv, “Second-harmonic generation with pulses in a coupled-resonator optical waveguide,” Phys. Rev. E **65**, 026607 (2002).

[29] S. Boscolo, M. Midrio, and C. G. Someda, “Coupling and Decoupling of Electromagnetic Waves in Parallel 2-D Photonic Crystal Waveguides,” IEEE J. Quantum Elect. **38**, 47-53 (2002).

[30] I. Park, H. S. Lee, H. J. Kim, K. M. Moon, S. G. Lee, B. H. O, S. G. Park, and E. H. Lee, “Photonic crystal power-splitter based on directional coupling,” Opt. Express **12**, 3599-3604 (2004).

[31] T. B. Yu, M. H. Wang, X. Q. Jiang, Q. H. Liao, and J. Y. Yang, “Ultracompact and wideband power splitter based on triple photonic crystal waveguides directional

coupler," J. Opt. A : Pure Appl. Opt. **9**, 37-42 (2007).

[32] A. Sharkawy, S. Shi, and D. W. Prather, "Electro-optical switching using coupled photonic crystal waveguides," Opt. Express **10**, 1048-1059 (2002).

[33] N. Yamamoto, T. Ogawa, and K. Komori, "Photonic crystal directional coupler switch with small switching length and wide bandwidth," Opt. Express **14**, 1223-1229 (2006).

[34] D. M. Beggs, T. P. White, L. O'Faolain, and T. F. Krauss, "Ultracompact and low-power optical switch based on silicon photonic crystals," Opt. Lett. **33**, 147-149 (2008).

[35] M. Qiu, M. Mulot, M. Swillo, S. Anand, B. Jaskorzynska, and A. Karlsson, "Photonic crystal optical filter based on contra-directional waveguide coupling," Appl. Phys. Lett. **83**, 5121-5123 (2003).

[36] F. S. S. Chien, Y. J. Hsu, W. F. Hsieh, and S. C. Cheng, "Dual wavelength demultiplexing by coupling and decoupling of photonic crystal waveguides," Opt. Express **12**, 1119-1125 (2004).

[37] F. S. S. Chien, S. C. Cheng, Y. J. Hsu, and W. F. Hsieh, "Dual-band multiplexer/demultiplexer with photonic-crystal-waveguide couplers for bidirectional communications," Opt. Commun. **266**, 592-597 (2006).

[38] K. M. Leung, and Y. F. Liu, "Full Vector Wave Calculation of Photonic Band Structures in Face-Centered-Cubic Dielectric Media," Phys. Rev. Lett. **65**, 2646-2649 (1999).

[39] S. G. Johnson, and J. D. Joannopoulos, "Block-iterative frequency-domain methods for Maxwell's equations in a planewave basis," Opt. Express **8**, 173-190 (2001).

[40] A. Taflove and S. C. Hagness, *Computational Electrodynamics: The Finite-Difference Time-Domain Method* (Artech House, Norwood, MA, 2000).

[41] H. Benisty, "Modal analysis of optical guides with two-dimensional photonic band-gap boundaries," J. Appl. Phys. **79**, 7483-7492 (1996).

[42] N. W. Ashcroft and N. D. Mermin, *Solid State Physics* (Sounders, Philadelphia, 1976).

[43] J. Callaway, *Quantum Theory of the Solid State* (Academic Press, Boston, 1991).

[44] M. Bass, *Handbook of Optics : Optical properties of materials, nonlinear optics, quantum optics* (McGraw Hill Professional, 2009).

[45] J. D. Joannopoulos, R. D. Meade, and J. N. Winn, *Photonic Crystals* (Princeton, 1995).